Aalto University
School of Engineering

Safi Ur Rehman

Finite Element Analysis of Impact-perforated Reinforced Concrete Slabs

Master Thesis submitted in partial fulfillment of the requirements for the degree of Master of Science in Structural Engineering and Building Technology.

Espoo, Date: 27.11.2017
Supervisor: Asst. Prof. Jarkko Niiranen
Advisor(s): M.Sc. Markku Raiskila, D.Sc. (Tech) Alexis Fedoroff

Aalto University
School of Engineering

Aalto University, P.O. BOX 11000, 00076 AALTO
www.aalto.fi

Abstract of master's thesis

Author	Safi Ur Rehman
Title of thesis	Finite Element Analysis of Impact-perforated Reinforced Concrete Slabs
Degree programme	Master's Programme in Structural Engineering
Major/minor	Structural Engineering/Construction Management **Code** ENG3039
Thesis supervisor	Assistant Professor Jarkko Niiranen
Thesis advisor(s)	M.Sc. Markku Raiskila, D.Sc. (Tech) Alexis Fedoroff
Date	27.11.2017 **Number of pages** 64 **Language** English

Abstract

The safety of the workers and durability of structures against the impact of low-velocity falling weights is of significant importance in construction industry, especially for construction of multi-storey buildings. The empirical formulae for the estimation of the impact behavior of reinforced concrete are limited to the domain settings in which they are generated and are originally developed for high-speed velocity impacts less relevant to the construction industry.

This study presents a finite element analysis procedure for the impact analysis of reinforced concrete slabs under low-velocity and high-mass impacts using the Abaqus/Explicit solver. A modified Concrete Damage Plasticity material model with strain rate effects and a physically motivated element deletion criterion has been used for modelling concrete and strain-rate-dependent elastoplastic damage model is utilized for modelling the reinforcement. A three dimensional Langrangian formulation and eight-node hexahedron elements with reduced integration are used for modelling concrete. The reinforcement is discretized with two-node beam elements. The numerical analysis is compared against three experimental impact tests carried out at Heriot-Watt University. In terms of perforation and the velocity-history of the impactor, the numerical results are found to be accurate.

The validated finite element procedure is then used to estimate the minimum velocity of the impactor required to perforate, in the sense of the so-called ballistic limit, a 150 mm thick two-layer reinforced concrete slab for impactor weights 250 kg, 500 kg and 1000 kg. The obtained ballistic limits are compared to the empirical formula of UK Atomic Energy Authority: a very good correlation has been obtained, adding a second layer of validation onto the numerical procedure.

Keywords Finite Element Method, Impact, Reinforced Concrete slab, Perforation, Concrete Damage Plasticity, Abaqus/Explicit

FOREWORD

The methodology of this thesis, roughly speaking, is the simulation of a real life event using computer tools which has presented a great interest to me since long. While I was a novice in the numerical analysis, this research provided me with an opportunity to learn, experience and add to the greater knowledge associated with the impact analysis. The whole process, though demanding at times, has left me with greater understanding of impact analysis, and has generally strengthened my attitude towards research. I feel proud to have been part of the greater picture of impact studies related to structures and look forward to further opportunities in the field.

In truth, this could not have been possible without my family back home, whose love and support continually instills more passion and energy in me. I dedicate this work to my great parents. Thank you dear *Ammi* and *Baba*, for supporting me, believing in me and making me who I am.

I am grateful to my supervisor Asst. Prof. Jarkko Niiranen for his supervision, guidance and understanding throughout this journey. He showed me the course I could take and presented me with ideas when I needed them and I am thankful to him for that.

I would also like to extend my gratitude towards my advisor Mr. Markku Raiskila for agreeing to provide assistance and supporting me shape the initial phase of the research. A special appreciation is extended to my second advisor Mr. Alexis Fedoroff and VTT Technical Research Finland for helping me out in the material modelling which greatly influenced this research.

This journey was possible because Mr. Aki Vuolio entrusted me with the responsibility in the first place. I am thankful to him and Ramboll Oy for providing the financial assistance for this project in collaboration with Aalto University, Department of Civil Engineering, serving as the site of research.

21.11.2017

Safi Ur Rehman

Safi Ur Rehman

Table of Contents

List of Figures

List of Tables

1. INTRODUCTION

The study of the impact phenomena is significant for the various fields of engineering and research. For example, military engineers need to study this phenomenon to make their designs so that they are able to endure the effects of projectile impact; automobile industry needs to understand it so that they could improve the safety of their products; and structural engineers have to take into account the effects of blasts, collisions, earthquakes and falling objects onto the structure for the safe and efficient design. During the construction of multistory buildings, the effects of falling weights resulting from accidents in construction industry e.g. in crane operations or other man-made disasters that result in impact loads on the structure needs to be considered. This poses a risk of safety for the workers on the lower floors as well as to the stability of the target structure. This chapter provides a brief background on the impact phenomenon related to the reinforced concrete structures then discusses the main objectives of this study.

1.1. Background

Reinforced concrete structures are undoubtedly the most common type of structures used in the construction industry. Various design codes throughout the world deal with the design of such structures under various normal routine load combinations. Some abnormal loads, however, are also of great significance in the design of concrete structures, which may arise in different situations, for example, blasts, earthquakes, the collision of trains, cars, planes and falling weights etc. The focus of this study is to study the effects of falling weights over the reinforced concrete slabs. The construction industry practices involve the risk that there could be a physical accident at some instance resulting from the failure of machinery or man-made mistakes. Such incident may cause the falling of objects from, say cranes, on the underlying structure and pose a threat to the safety of the workers or the durability of the structure where it makes an impact.

Reinforced concrete, although used very extensively, has very complex material behavior. This complexity arises from non-linearity in the stress-strain relation, tensile cracking, different strain hardening/softening relation in tension and compression, stiffness degradation, the bond between the concrete and the reinforcement. Furthermore, the strain rate dependency and confinement dependency in dynamic loading situations may further add to the complexity of modeling its material behavior.

The impact loadings cause local and global deformations in the target structure. The local deformations are restricted to the vicinity of the impact zone for example concrete plug formation, crushing, scabbing etc. The global effects may be large deformations that may result in bending failure. There are various approaches for investigating the effects of concrete. Experimental tests are one way, but it is expensive and usually results in empirical formulae, which cannot be generalized for different cases than the ones for which these formulae are

generated. The numerical methods, for example, finite element method, however, can be used to study the behavior of reinforced concrete under impacts capturing both the local and global effects of the impacts in a cost-efficient way. The literature review provides a short overview of the experimental tests and the numerical studies of the impact of the reinforced concrete slabs.

1.2. Objectives

The main objective of the thesis is to develop a finite element procedure that can be used to analyze the behavior of reinforced concrete slabs under low-velocity impacts, which are more relevant to the construction industry. An important part of this process is the selection of a suitable concrete material model that could successfully capture the various complexities of the concrete material behavior. With the main objective in mind, the following investigations are carried out in this study.

- Literature review related to the behavior of reinforced concrete slabs subject to impact loadings.

- The study of the various concrete material models suitable for impact analysis and their common applications.

- Validation of the chosen material model for low-velocity impact analysis by comparing the analysis results with the experimental tests.

- Further numerical impact studies based on the validated finite element procedure for a two-layer reinforced concrete structure, which is more closely related to the construction industry context.

- Comparison of the results from the two-layer reinforced concrete slab with an empirical formula.

2. LITERATURE REVIEW

2.1. Introduction

The effects of the missile impact on a concrete target have been studied since the mid-1700s mainly because of the military sector's interest in the design of more durable protective barriers as well as to develop high performance missiles. Missile impacts can be categorized as hard or soft. In the Hard missile impact, the deformation of the missile is insignificant as compared to the deformation of the target while in soft impact the missile itself deforms significantly as well. Although the research about the impact behavior of reinforced concrete structures was mainly triggered by the military sector, the development of the nuclear reactor industry increased the research in this area more dramatically. When a reinforced concrete structure is subjected to the impact loading, the most common responses that the structure may have depending on the kind of impact are classified as follows. (Jabbar *et al.*, 2011)

Local response: Energy dissipation is concentrated around the impact region it generates local effects e.g. shear plug formation, scabbing etc.

Global response: The bending and deformation of the whole member.

Combined response: Combination of the local and global response.

The different phenomenon in these responses associated with the impact on reinforced concrete targets are explained with Figure 1 as follows (Li *et al.*, 2005)

a) **Penetration:** Tunneling into the target by the projectile (the length of the tunnel is called the penetration depth).

b) **Cone cracking and plugging:** Formation of a cone-like crack under the projectile and the possible subsequent punching-shear plug.

c) **Spalling:** Ejection of target material from the proximal face of the target.

d) **Radial cracking:** Global cracks radiating from the impact point and appearing on either the proximal or distal face of the concrete slab or both, when cracks develop through the target thickness.

e) **Scabbing:** Ejection of fragments from the distal face of the target.

f) **Perforation:** Complete passage of the projectile through the target with or without a residual velocity.

g) **Overall structural responses and failures:** Global bending, shear and membrane responses as well as their induced failures throughout the target.

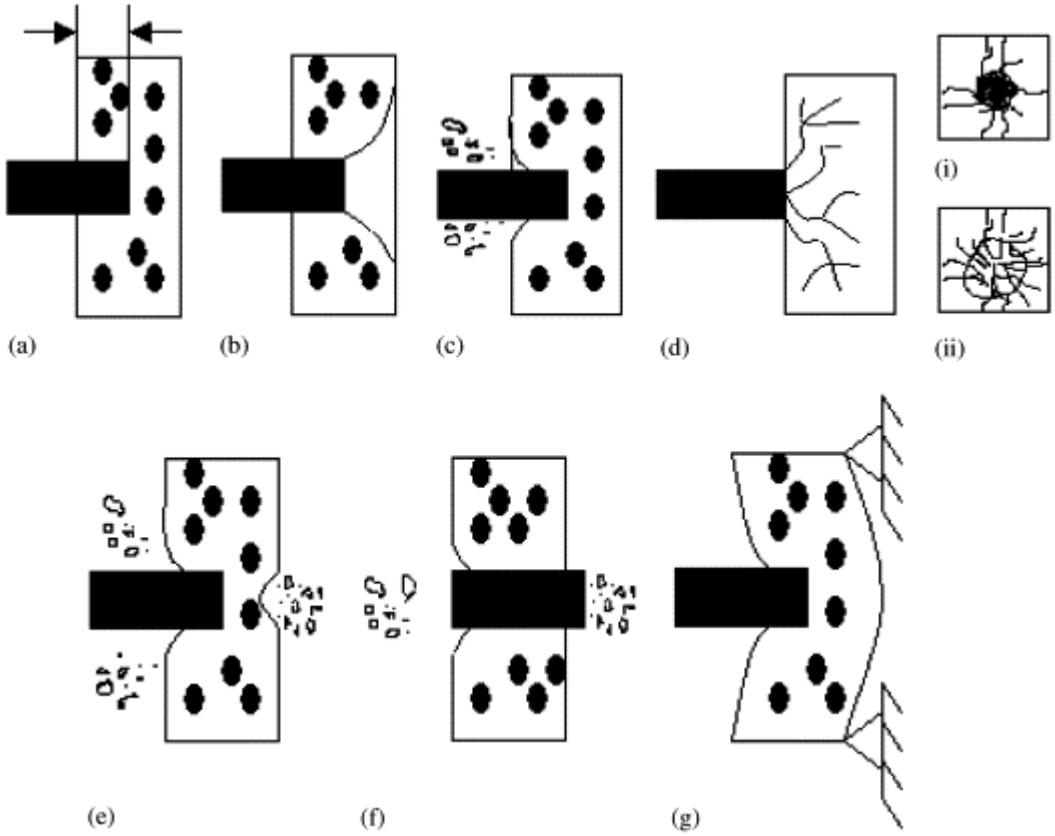

Figure 1 Missile impact effects on concrete target, (a) Penetration, (b) Cone cracking, (c) Spalling, (d) Cracks on (i) proximal face and (ii) distal face, (e) Scabbing, (f) Perforation, and (g) Overall target response. (Li et al., 2005)

Among these phenomena, spalling, penetration, scabbing, cone cracking and perforation are considered as local effects and are quantified by the following measurements (Li *et al.*, 2005)

Penetration depth (x)**:** The depth to which a projectile penetrates into a massive concrete target without perforation.

Scabbing limit (hs)**:** The minimum thickness of the target required to prevent scabbing.

Perforation limit (e)**:** The minimum thickness of the target required to prevent perforation.

Ballistic limit (VBL)**:** The minimum initial impact velocity that will perforate the target.

2.2. Concrete Slabs under Impact Loads

The three important approaches of studying the impact behavior of reinforced concrete are experimental, analytical and numerical methods. Li *et al.*, (2005) presents the analytical model developing a formulation of the penetration resistance of a target. This section presents a brief overview of experimental and numerical studies of the impact behavior of the reinforced concrete slabs.

Reinforced concrete slabs are mostly subjected to the local damage due to the impact loadings or at least that is the most critical phenomenon for investigation. Since the beginning of the impact related studies, a large number of experimental studies have been performed to study the local effects of hard projectiles on the reinforced concrete structures (mostly slabs).These generated large number of empirical formulae. The main variables in question in most of these empirical formulas are penetration depth, scabbing and perforation limits. Li *et al.*, (2005) and Kennedy, (1976) have presented a summary of empirical formulae generated based on the wide range of experiments. These empirical formulae, however, are limited to a specific range since they are based on curve fitting data and most of them are unit-dependent and limited by the range of validity, only suitable within the range of tests from which the data is acquired. In addition, the local effects predicted by these formulae are independent of the global response of the member, i.e. bending and shear. However, the global response might affect the local response in low-velocity impacts (Li *et al.*, 2005). One of the empirical formulae for predicting the ballistic limit, based on what is known as CAE-EDF formula, is used for comparison with the ballistic limits obtained numerically in this study.

The numerical methods have several advantages over the analytical methods and empirical formulae developed based on experimental tests. They are cost effective and can determine the local response of the target along with the global response. Discrete element method (DEM), Smoothed-particle hydrodynamics (SPH) and Finite Element Method (FEM) are the commonly used numerical methods for carrying out the impact analysis. Shiu, Donze and Daudeville, (2009) have used the DEM to study the penetration and perforation process of a reinforced concrete target slabs subject to missile impacts. Terranova, Schwer and Whittaker, (2017) have used an Axisymmetric SPH model to perform a parametric study of the wind-borne missile impacts on the reinforced concrete structures. Finite element methods, however, remains the most commonly used numerical method for the impact analysis and is the adopted methodology in this study. The first attempt to apply the finite element method to a reinforced concrete structure was made by Scordelias and Ngo, (1967). With time, the numerical simulations of dynamic analysis became more important for structural design subjected to impact and blast loads. Some of the wide range of numerical simulations carried out using finite element method to predict the impact behavior of concrete slabs are discussed below.

Miyamoto et al., 1991 used the Dracker-Prager model for concrete modelling when comparing the numerical and analytical response of the reinforced concrete slabs under impulse loads. Shirai et al.,1997 used the DYNA-3D software package, now called LS-DYNA, to simulate the nonlinear behavior of doubly layered reinforced concrete slab.

Ågårdh and Laine, (1999) carried out the 3D simulation of steel projectile perforation through 60 mm thick reinforced concrete slab. He used the LS-DYNA to simulate the impact involving a velocity of 1500 m/s. The material model used is 78 “Soil/concrete” with the erosion, which is available in the LS-Dyna material library. The results were compared with the tests and were found to be fairly well in agreement in terms of the the exit velocity of the impactor and the diameter of the exit crater in the slab. However, more studies were deemed necessary to assess the sensitivity of certain material parameters.

Algaard, Lyle and Izatt, (2005) and Izatt *et al.*, (2009) have used the LS-DYNA to model the non-linear material behavior for both steel and concrete. They simulated the experimental tests carried out at Heriot-Watt University to analyze the impact behavior of slabs to low velocity impacts. The results were compared with the experimental tests and with the empirical results and good agreement was found on the perforation limits. The experimental tests of an I-section impacting with different velocities in Izatt *et al.*, (2009) are used in the validation study in this thesis.

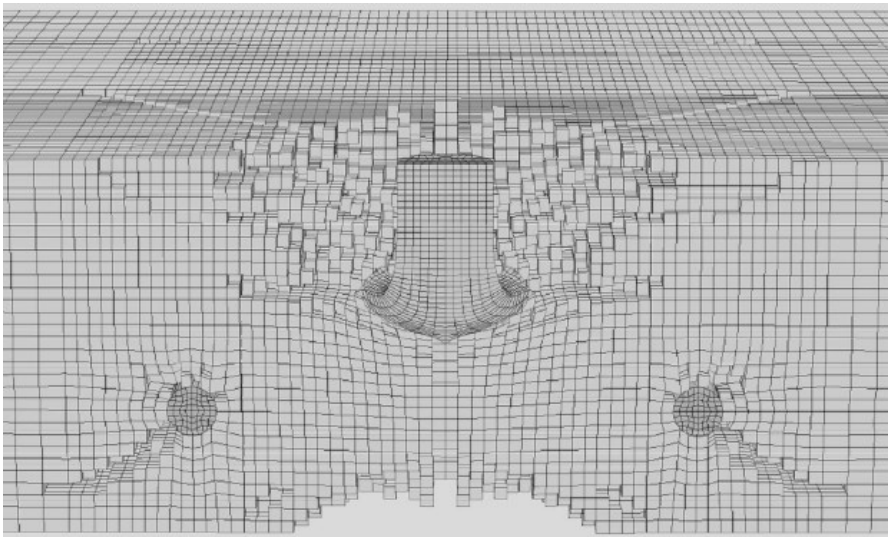

Figure 2 The impactor fragment perforating the concrete slab as the material becomes eroded. (Ågårdh and Laine, 1999)

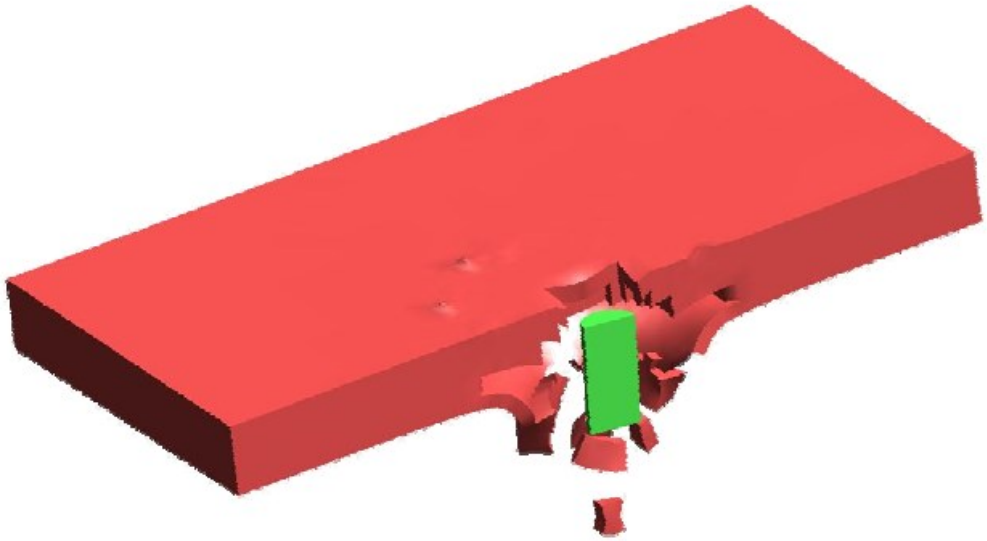

Figure 3 A 500 kg solid projectile perforating a 200 mm Reinforced concrete slab. (Algaard, Lyle and Izatt, 2005)

Jabbar *et al.*, (2011) have used the Winfrith concrete model in LS-DYNA to simulate the impact behavior of another set of experimental tests carried out at Heriot-Watt university (Chen and May, 2009). The experiments had different weights of a cylindrical impactor falling over three different sizes of reinforced concrete slabs. The main results that were compared

between the tests and the numerical analysis included the crack pattern on the slab and the impact force history. The crack pattern were found to have good agreement, however, the impact force history was not well matched with the experiment. Mokhatar and Abdullah, (2012) have simulated one of these experimental tests in Abaqus using different material models and the results were satisfactory about the impact force history. However, no satisfactory comparison of the crack patterns or the damage was provided.

Improving Robustness Assessment Methodologies for Structures Impacted by Missiles (IRIS) benchmark project (Vepsä *et al.*, 2012) led to a large number of impact simulations of hard and soft missile impact on the reinforced concrete structure tests. This project focused on improving the robustness of assessment methodologies for high-speed missile impacts in the context of safety for nuclear facilities. Different experimental tests were carried out for understanding the bending, punching and combined punching and bending behavior of reinforced concrete walls under impact loading. The test for assessing the combined behavior was carried out in Meppen, German whereas all the other tests were carried out by VTT Technical Research Centre of Finland. Using the data obtained from these tests, a large number of computer simulations by using different tools and material models were made. A more detailed information about these studies could be obtained from the reports OECD-NEA, (2012) and OECD-NEA, (2014).

3. FINITE ELEMENT MODELLING

3.1. Introduction

Various numerical methods can be used to perform impact analysis of reinforced concrete structures. The finite element method is one of the most useful numerical method for analyzing engineering problems. Its emergence has made possible to model and analyze a very wide spectrum of problems in various fields of engineering. The FEM software Abaqus is used in this study. Abaqus/Explicit solver is used for the solution of the dynamic equilibrium equations. A brief generalized dynamic equilibrium equation for a continuum is derived and other salient features of the software are discussed that are more relevant and particular to our study in this section.

3.2. Generalized Finite Element Formulation for Non-linear Structural Dynamics

To start with the study of a simple dynamics problem, consider the single degree of freedom system as shown in Figure 4 below. It has a mass m, stiffness constant of the spring is k and damping is represented by c_v.

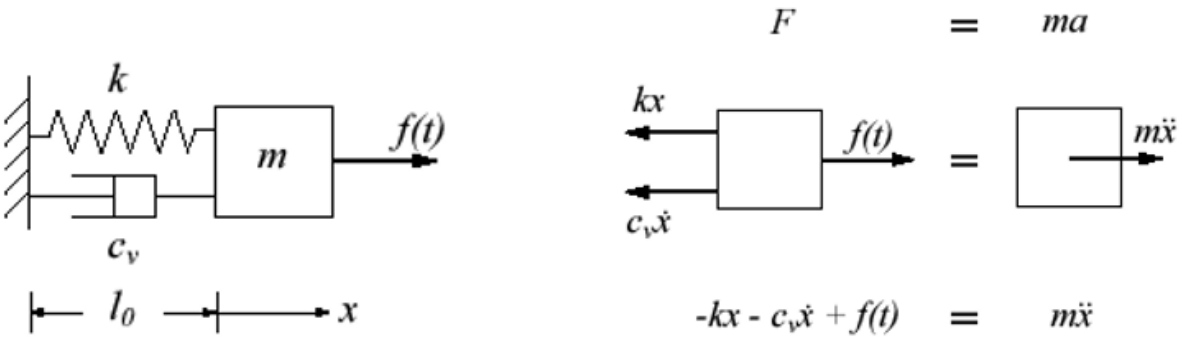

Figure 4 A single degree of freedom system under dynamic loading.

By using the Newton's second law of motion and the equilibrium of forces, the equation of motion for this system can be written as

$$m\ddot{x}(t) + c_v\dot{x}(t) + kx(t) = f(t) \tag{3.1}$$

where $x = x(t)$ denotes the displacement. The general governing equation for structural dynamics is the extension of the same principle to a three dimensional case. For a three dimensional problem, the governing equation can be derived based on the principle that external work done by the applied loads is equal to the work absorbed by inertial, dissipative and internal forces for any virtual displacement (any small motion which satisfies the compatibility and essential boundary conditions). This work balance, for an element of volume V and surface area S can be written as (Cook, Malkus and Plesha, 1989):

$$\int_V \delta \boldsymbol{u}^T \boldsymbol{F} dV + \int_S \delta \boldsymbol{u}^T \boldsymbol{\Phi} dS + \sum_{i=1}^{n_p} \delta \boldsymbol{u}_i^T \boldsymbol{p}_i = \int_V (\delta \boldsymbol{u}^T \rho \ddot{\boldsymbol{u}} + \delta \boldsymbol{u}^T c \dot{\boldsymbol{u}} + \delta \boldsymbol{\varepsilon}^T \boldsymbol{\sigma}) dV \qquad (3.2)$$

Where $\boldsymbol{F}$ and $\boldsymbol{\Phi}$ represents the body forces and the surface traction, $\boldsymbol{p}_i$ and $\delta \boldsymbol{u}_i$ represent the concentrated forces and their virtual displacement, respectively, at n_p number of points. c is the damping parameter and ρ is the mass density. $\delta \boldsymbol{u}$ represent the virtual displacement and $\delta \boldsymbol{\varepsilon}$ represents the respective strains. When finite element discretization is applied, the shape functions $\boldsymbol{N}$ are dependent on space variables whereas the degrees of freedom $\boldsymbol{d} = \boldsymbol{d}(\boldsymbol{t})$ are dependent on time. We thus have then

$$\boldsymbol{u} = \boldsymbol{N}\,\boldsymbol{d} \qquad \dot{\boldsymbol{u}} = \boldsymbol{N}\,\dot{\boldsymbol{d}} \qquad \ddot{\boldsymbol{u}} = \boldsymbol{N}\,\ddot{\boldsymbol{d}} \qquad \boldsymbol{\varepsilon} = \boldsymbol{B}\,\boldsymbol{d} \qquad (3.3)$$

Combining equations (3.2) and (3.3) yields,

$$\delta \boldsymbol{d}^T \left[\int \rho\, \boldsymbol{N}^T \boldsymbol{N}\, dV\, \ddot{\boldsymbol{d}} + \int c\, \boldsymbol{N}^T \boldsymbol{N}\, dV\, \dot{\boldsymbol{d}} + \int \boldsymbol{B}^T \boldsymbol{\sigma}\, dV - \int \boldsymbol{N}^T \boldsymbol{F} dV - \int \boldsymbol{N}^T \boldsymbol{\Phi}\, dS - \sum_{i=1}^{n} \boldsymbol{p}_i \right] = 0 \qquad (3.4)$$

The first two integrals excluding the derivatives of $\boldsymbol{d}$ form the "consistent" mass and damping matrices:

$$\boldsymbol{M} = \int \rho\, \boldsymbol{N}^T \boldsymbol{N}\, dV \qquad (3.5)$$

$$\boldsymbol{C} = \int c\, \boldsymbol{N}^T \boldsymbol{N}\, dV \qquad (3.6)$$

The word "consistent" means that same shape functions are used in the mass and damping matrices as in the stiffness matrix.

The third integral represents the vector of internal forces (or moments), i.e., the internal resistance to the applied stresses on the element.

$$\boldsymbol{r_{int}} = \int \boldsymbol{B}^T \boldsymbol{\sigma}\, dV \qquad (3.7)$$

$$\boldsymbol{r_{ext}} = \int \boldsymbol{N}^T \boldsymbol{F} dV + \int \boldsymbol{N}^T \boldsymbol{\Phi}\, dS + \sum_{i=1}^{n} \boldsymbol{p}_i \qquad (3.8)$$

The equation (1.4), if it is to be true for an arbitrary $\delta \boldsymbol{d}^T$, then becomes

$$\boldsymbol{M}\ddot{\boldsymbol{d}} + \boldsymbol{C}\dot{\boldsymbol{d}} + \boldsymbol{r_{int}} = \boldsymbol{r_{ext}} \qquad (3.9)$$

This equation is true for linear and non-linear problems. Generally for a linear problem, $\boldsymbol{r_{int}} = \boldsymbol{Kd}$ whereas for a non-linear problem $\boldsymbol{r_{int}} = \boldsymbol{K(d)d}$. The matrix $\boldsymbol{K}$ denotes the stiffness matrix. The dependency of $\boldsymbol{K}$ on $\boldsymbol{d}$ arises in geometrical non-linearity from the consideration of the second order terms of strains.

A more general equation for the dynamics of a flexible non-linear structure including geometrical, material and non-linearity arising from boundary conditions e.g. impact force can be written as:

$$\boldsymbol{p}_{inertial}(\boldsymbol{d}, \dot{\boldsymbol{d}}, \ddot{\boldsymbol{d}}, t) + \boldsymbol{p}_{damping}(\boldsymbol{d}, \dot{\boldsymbol{d}}, t) + \boldsymbol{p}_{elastic}(\boldsymbol{d}, \dot{\boldsymbol{d}}, t) = \boldsymbol{r}(\boldsymbol{d}, t) \qquad (3.10)$$

where $\boldsymbol{p}_{inertial}$, $\boldsymbol{p}_{damping}$ and $\boldsymbol{p}_{elastic}$ represent the vectors corresponding to inertial, damping and internal resistance effects respectively. $\boldsymbol{r}(\boldsymbol{d}, t)$ is the external force vector which in this case is dependent on $\boldsymbol{d}$ as could be the case in an impact problem or other contact problem.

3.3. Solution Procedures for the Governing Equations

The equilibrium equation discussed in section 3.2 is a second order differential equation. It can be solved using implicit or explicit procedures depending on the type of the problem being analyzed. The impact phenomenon involves large deformations, non-linear material response and contact boundary condition which makes the use of implicit method undesirable and very expensive because of expensive inversion of the stiffness matrix especially in large models. The explicit methods, on the other hand, can handle these behaviors more efficiently.

Abaqus/Explicit is a finite element analysis product that is well suited for the simulation of dynamic events. It can handle a large number of increments using the explicit central-difference time integration rule which is explained below. Each increment is inexpensive as compared to the implicit solver because there is no need to solve for a set of simultaneous equations.

Time Integration in Abaqus/Explicit Solver

The explicit dynamic analysis procedure in Abaqus/Explicit is based on the application of explicit central-difference time integration rule along with the use of lumped element mass matrices. The explicit time integration rule itself does not provide the efficiency associated with explicit dynamics procedure. The key to the computational efficiency is the use of lumped mass element matrices whose inverse is easily computed and the multiplication of the mass inverse by the inertial force needs only n operations, where n is the number of degrees of freedom. The explicit procedure requires no iterations and no tangent stiffness matrix. (ABAQUS manual).

The use of lumped mass matrix makes it efficient to calculate the nodal acceleration $\ddot{u}^N_{(i)}$ from the equilibrium equation at the current increment i in the explicit dynamic step.

$$\ddot{u}^N_{(i)} = (M^{NJ})^{-1}\left(P^J_{(i)} - I^J_{(i)}\right) \qquad (3.11)$$

Where M^{NJ} is the mass matrix, P^J is the external load vector coming from the external sources (e.g. body forces , tractions etc.) and I^J is the internal force vector getting contributions from resisting stress, damping, viscosity, and hourglass control.

Once the acceleration are known, central-difference integration scheme is then used to progress the kinematic state by calculating the velocity at $i+\frac{1}{2}$ and displacement (degree of freedom $u^N_{(i+1)}$) at $i+1$:

$$\dot{u}^N_{(i+\frac{1}{2})} = \dot{u}^N_{(i-\frac{1}{2})} + \frac{\Delta t_{(i+1)}+\Delta t_{(i)}}{2}\ddot{u}^N_{(i)} \tag{3.12}$$

$$u^N_{(i+1)} = u^N_{(i)} + \Delta t_{(i+1)}\dot{u}^N_{(i+\frac{1}{2})} \tag{3.13}$$

From the displacement, we obtain strains in the next increment, i.e., $i+1$, which in turns gives element stress, and then again, this cycle is repeated by calculation of acceleration from equation (3.11) for the next increment $i+1$.

Time Increments

The explicit central difference integration is a conditionally stable operation. The maximum time increment has to be small enough to yield a stable solution. This stability limit for the time increment in terms of the maximum frequency ω_{max} of the system (with no damping) is given as (ABAQUS manual).

$$\Delta t \leq \frac{2}{\omega_{max}} \tag{3.14}$$

Generally, determination of the maximum frequency of the system is a complex procedure with computational expenses (Jabbar *et al.*, 2011). Therefore, an approximation of the stability limit is often written as the smallest transit time taken for a dilatational wave to travel across the smallest element of the domain, i.e.

$$\Delta t \leq \frac{L_{\min}}{c_d} \tag{3.15}$$

where $L_{\min}$ is the smallest dimension of an element and c_d is the speed of the dilatational wave.

Abaqus/Explicit calculates the dilatational wave speed c_d from the effective hypoelastic material moduli based on the material's constitutive behavior. For an isotropic, elastic material it can be calculated in terms of Young's modulus E, Poisson's ratio υ and material density ρ as

$$c_d = \sqrt{\frac{E(1-\upsilon)}{(1+\upsilon)(1-2\upsilon)\rho}} \tag{3.16}$$

3.4. Discretization of Reinforced Concrete

A three-dimensional model is used in the finite element analysis to capture the local and global effects of the impact on the reinforced concrete. The discretization of the three dimensional model in transient problem is usually performed using hexahedral or tetrahedral solid elements.

C3D8R Hexahedral Element

In this study, concrete is discretized using the first order, reduced integration, eight-node hexahedral elements C3D8R from Abaqus/Explicit element library. Reduced integration uses lower-order integration (one-point integration) to form the element stiffness. The reduced integration decreases the time of the computation and increases efficiency especially in three dimensions. The use of first-order, reduced integration elements also prevents the shear and volumetric locking which can be a problem in first order fully integrated elements, e.g. C3D8.

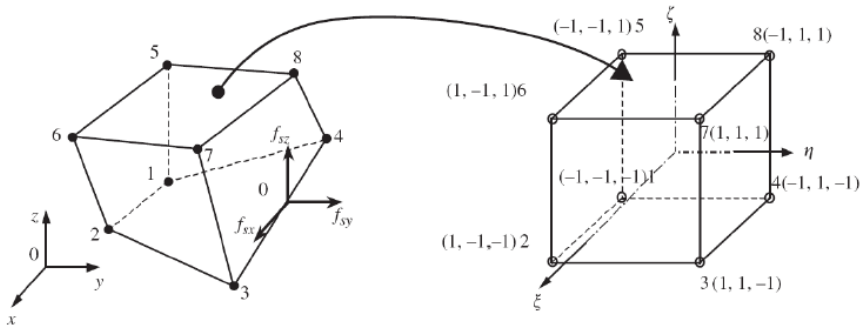

Figure 5 Eight node hexahedron element (Jabbar *et al.*, 2011)

Hourglassing

First order, reduced integration are computationally very efficient. However, these elements can undergo hourglassing. Since the elements have a single integration point at the center of the element, such distortions of the element could occur that does not produce any strains at the integration point and so we obtain uncontrolled distortion of the elements known as the hourglassing (Abaqus, Manual). Hourglass controls in Abaqus/Explicit can be used to overcome the hourglassing modes. These formulations introduce an artificial stiffness or viscous damping into the system to overcome the hourglassing.

For C3D8R elements, Abaqus, by default, uses relax stiffness formulation for hourglass control. This works well with most of the simulations performed in this study. However, it is computationally very intensive. Viscous hourglass formulations are recommended for high velocity/strain rates and they are the least computationally intensive. The artificial energy (energy associated with the hourglass modes) needs to be bounded and be a small portion (10% as a rule of thumb) of the total internal energy of the system. However, this rule of thumb could vary for different types of problems and material models. The final call lies with the engineer to decide whether the hourglass energy is too high and whether it affects the simulation results.

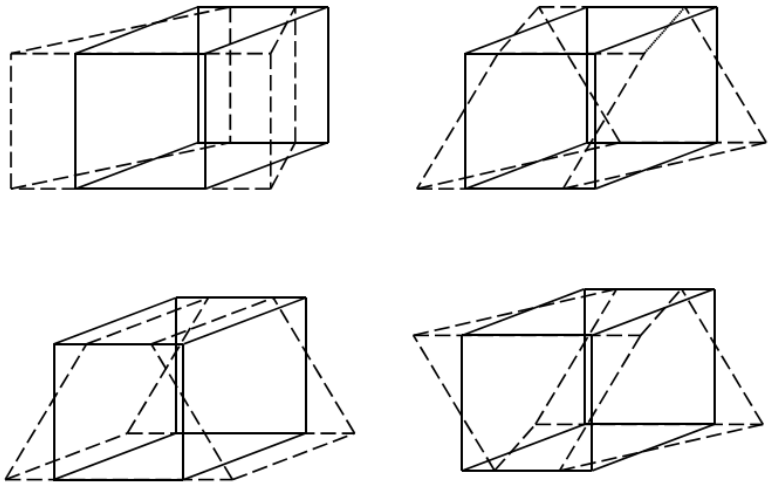

Figure 6 Four hourglass modes of an eight node reduced integrated element. (Belytschko et al, 2000)

3.5. Discretization of Reinforcement

The reinforcement is commonly modelled using beam or truss elements. Since our simulations include bending, modelling reinforcement using beam elements made more sense. Abaqus offers different techniques for modelling the reinforcement. The most commonly used methods are the so-called discrete method and the embedded elements method. The discrete method can be utilized by using the stringers functionality in Abaqus, which can be used to assign the beam elements to the defined internal edges of the solids. This approach has the drawback that the mesh discretization is governed by the location of the reinforcement, as there needs to be common nodes between the reinforcement and solid sections. This drawback, however, is overcome by the use of embedded elements method. The embedded elements technique constrains the nodes of the embedded elements to the solid host sections without the need for

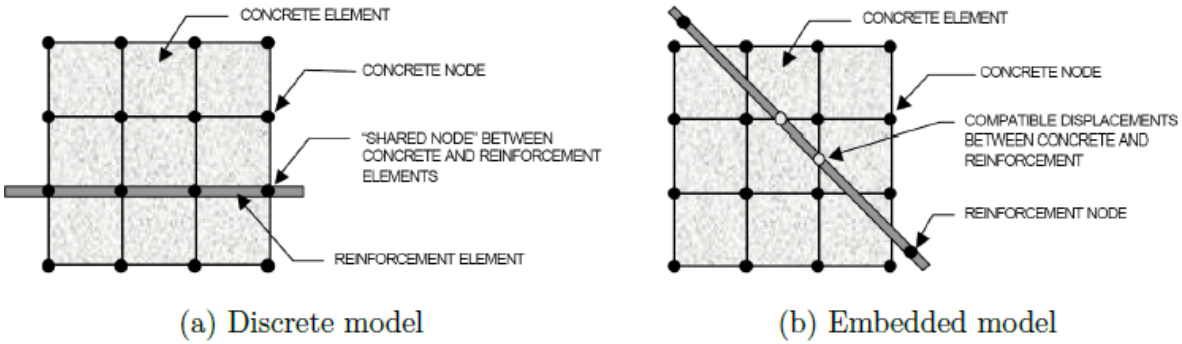

Figure 7 Reinforcement models in concrete (Tavarez et al., 2001)

node sharing. The original degrees of freedom of the embedded nodes are eliminated and they are constrained to the interpolated values from the degrees of freedom of the host element. The embedded element method is mentioned to be the preferred method for defining reinforcement in a solid (Abaqus, Manual).

3.6. Contact Modelling

Abaqus/Explicit uses two methods for the contact constraints enforcement, the penalty contact algorithm and kinematic contact algorithm. The fundamental differences between these two algorithms are briefly explained with the help of Figure 8.The figure shows a slave node, which will experience contact with a fixed master surface.

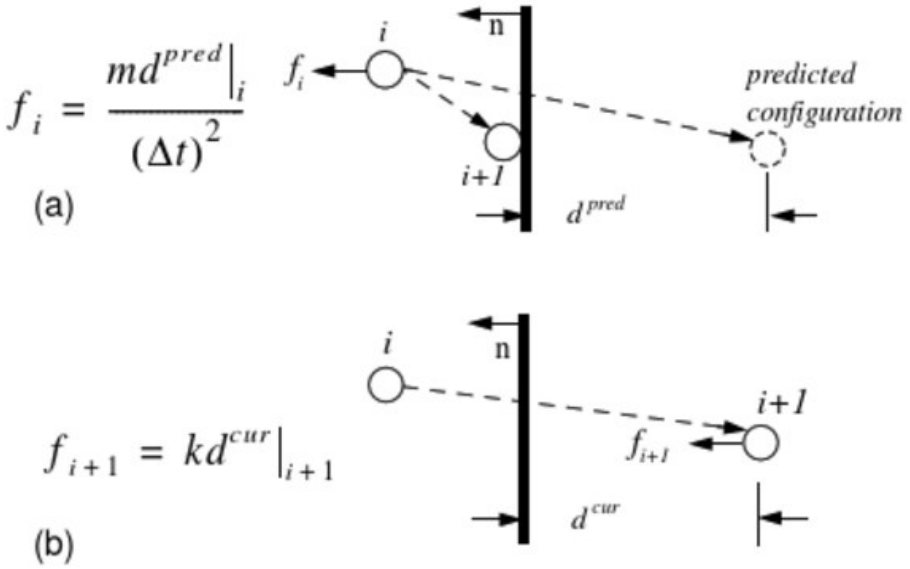

Figure 8 (a) Kinematic Contact, (b) Penalty Contact

The kinematic contact algorithm is a predictor/corrector method, i.e., Abaqus/Explicit goes through a predictor and corrector phase in each time increment when the contact is active. The predictor phase determines that overclosure or penetration and in the corrector phase, the master and slave nodes are corrected by applying acceleration corresponding the penetration predicted in the predictor phase. It can be viewed as an implicit method since the penetration is taken care of at the end of each increment, e.g., the penetration starting at the increment i is taken care of at the start of the new increment i+1.

The penalty contact algorithm is explicit in the sense that the penetration occurring in the increment i is taken care of in the increment i+1 by applying a spring interface between the nodes of slave and master surface to minimize the penetration. Abaqus/Explicit automatically computes a default interface spring stiffness using the stiffness and mass of the bodies coming to be in contact. This added stiffness can influence the stable time increment since this added stiffness is essentially taken as increased stiffness of the material.

In Abaqus/Explicit, the contact can be defined using the general contact or contact pair algorithm. The general contact algorithm is more robust and can use only penalty constraint enforcement method. It can have multiple contact domains with a single definition that can be detected automatically. It can also be very useful for defining contact when one or both the contacting bodies are eroding since the erosion would allow for the contact with the internal surfaces, which are only allowed in the general contact formulation currently.

The contact-pair algorithm can use both penalty and kinematic constraint enforcement methods but it doesn't support the internal surface generation for the accurate contact modelling in case of erosion. To overcome this, contact pair algorithm can be used with a node-based surface for the eroding body to allow for the internal surface contact. However, this does not lead to more accurate results (Abaqus, Manual).

4. CONSTITUTIVE MODELLING

Successful simulation of the material behavior requires the use of material models that are as accurate as possible for the application that it is used for. This chapter presents a discussion about three material models that are commonly adopted for the numerical simulation of concrete in commercial software. The first two material models, KCC (Karagozian & Case Concrete) Model and Winfrith Concrete Model**,** are available in LS-Dyna software package and are one of the most common material models used for the simulation of impact problems. The third model is the modification of the CDP (Concrete Damage Plasticity) available in Abaqus and is adopted in this study. In the end, this chapter presents the material model of the reinforcement adopted for this study.

4.1. Constitutive Modelling of Concrete

Concrete is a complex material to model. Successful modelling of concrete would require simulation of the various behaviors of concrete over a wide range of circumstances. This includes the behaviors shown by the small specimens of concrete up to full-scale structures. This also includes successful capturing of the rate-dependence of concrete behavior and the effects of confinement. Kouhia, (2013) has reviewed the basic concepts and mechanical features associated with concrete material models. He has also summarized the various pressure dependent failure criteria like Rankine, Durcker-Prager and the Mohr-Coulomb.

Since concrete is a pressure-dependent material, the general shape of failure surface for the pressure dependent materials can be written as

$$F(I_1, J_2, J_3) = 0 \tag{4.1}$$

Where I_1 $(= \sigma_{kk} = \mathbf{tr}(\boldsymbol{\sigma}))$ is the first invariant of stress tensor $\boldsymbol{\sigma}$. J_2 $(= \frac{1}{2} s_{ij} s_{ji} = \frac{1}{2}\mathbf{tr}(\boldsymbol{s}^2))$ and $J_3 (= \frac{1}{3} s_{ij} s_{jk} s_{ki} = \frac{1}{3}\mathbf{tr}\,(\boldsymbol{s}^3)$ are the second and third invariants of the deviatoric stress tensor $\boldsymbol{s}$. I_1 corresponds to the volumetric response whereas J_2 and J_3 corresponds to the deviatoric responses. The primary difference between various concrete constitutive models is how the volumetric and deviatoric responses are characterized. (Wu, Crawford and Magallanes, 2012)

Strain Rate Dependency

If a quasi-static concrete compression and tensile test data is used to model the concrete for dynamic simulations, it does not behave as expected (Fedoroff, Kuutti and Saarenheimo, 2017).

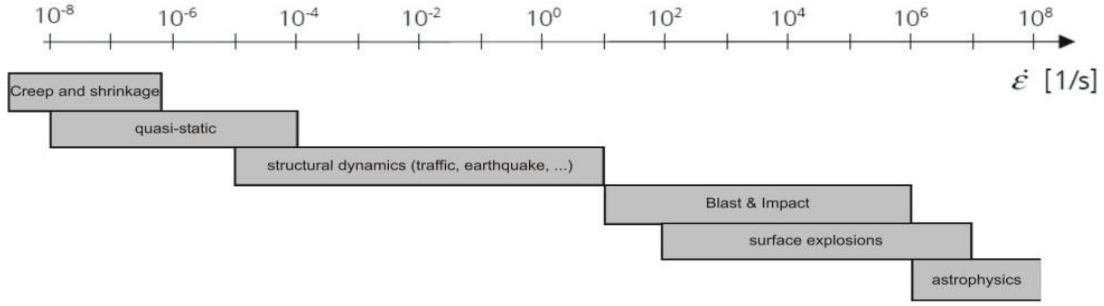

Figure 9 Strain rates for various events, (fib, 2010)

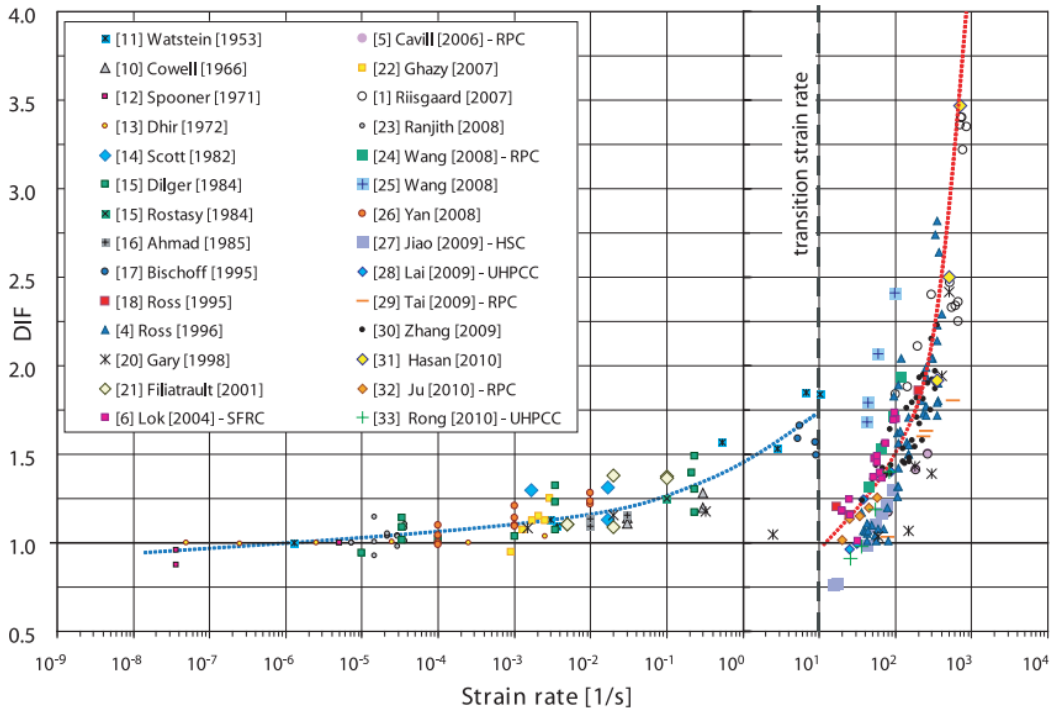

Figure 10 Strain Rate effect on compressive strength of concrete. (PAJĄK, 2011)

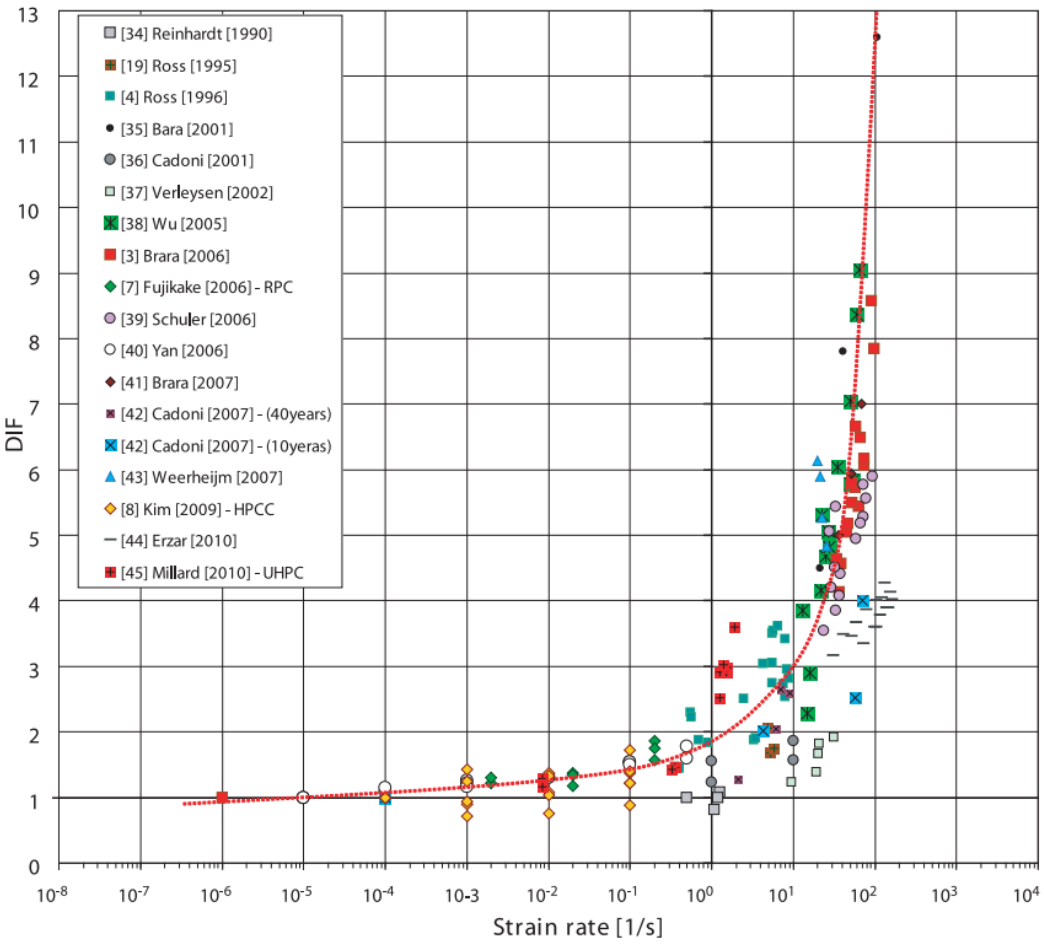

Figure 11 Strain rate effect on tensile strength of concrete (PAJĄK, 2011)

The reason is that concrete is a strain rate dependent material and the Dynamic Increase Factor (DIF) plays a non-trivial role in the events where high strain rates are involved. The impacts

generally have a strain rates varying from about 1 s^{-1} to 10 s^{-1} whereas blasts could have even higher rates as shown in Figure 9.

There is a significant experimental data for the scientific community to agree over the fact that concrete is a strain rate dependent both in axial compression and tension. Figure 10 shows the summary of the available test data on (mainly) concrete subjected to compression tests (PAJĄK, 2011). The results are shown as DIF vs strain rate. DIF is defined as the ratio of the dynamically increased strength to the quasi-static strength. Similarly, Figure 11 shows the strain rate effects on the tensile strength of concrete.

Although the consensus seems to have reached about the concrete being strain rate dependent, the physical phenomenon about why this change in strength happens is still not very clear. Confinement effect, capillary forces due to the pore pressure of water content and other fracture mechanics based considerations have been proposed for the dynamic increase of concrete properties and are discussed later in Section 4.4.2.

It is therefore important to include the strain rate effects in the material models for the study of dynamic problems.

4.2. KCC (Karagozian & Case Concrete) Model - MAT072

This model was developed in 1990s for use in the Finite Element code DYNA3D for analyzing structures subjected to blast and impact loading. Its latest release MAT_072R3 includes damage and strain rate effects. It has the capability of generating the parameters needed just by providing the unconfined compressive stress and density of concrete. It has been used for the analysis of structures subjected to quasi-static, blast, impact loads (Wu, Crawford and Magallanes, 2012). The model has three failure surfaces, which can be given in the generalized form as

$$\Delta\sigma_i = a_{0i} + \frac{p}{a_{1i}+a_{2i}.\,p} \tag{4.2}$$

where i stands for *m*, *y* and *r* i.e. the maximum strength surface, the yield surface and the residual strength surface. P denotes the hydrostatic pressure.The surfaces are defined by parameters $a_{ij,}$ which can be calibrated from the test data. The failure surface is obtained from interpolation among these three failure surfaces according to the following conditions.

$$\Delta\sigma_y \le \Delta\sigma \le \Delta\sigma_m : \Delta\sigma = \eta\left(\Delta\sigma_m - \Delta\sigma_y\right) + \Delta\sigma_y \tag{4.3}$$

$$\Delta\sigma \ge \Delta\sigma_m : \Delta\sigma = \eta(\Delta\sigma_m - \Delta\sigma_r) + \Delta\sigma_r \tag{4.4}$$

where $\Delta\sigma$ represents the active failure surface based on the deviatoric stress part and is given as

$$\Delta\sigma = \sqrt{3J_2} = \sqrt{\frac{3}{2}(s_{ij}s_{ji)}} \tag{4.5}$$

In the equation, η denotes the interpolation function depending on the modified effective plastic strain or internal damage parameter λ, which is a function of the 2nd invariant of the deviatoric stress tensor J_2. This function varies between 0 and 1 at λ=0 and $\lambda = \lambda_m$ respectively. This necessarily shows that the failure surface starts at the yield surface (point A in Figure 12) and then it moves towards the maximum strength surface (point B in Figure 12) as the internal damage parameter λ reaches the λ_m. This response mimics the hardening response. After that it comes back to the residual surface (point C in Figure 12) as λ reaches its maximum value resembling the softening response of the concrete. The relation between λ, λ_m and η is calibrated from experimental data. Figure 12 shows three meridians of the three failure surfaces in compression and tension. On the right hand side, the uniaxial stress-strain relationship going through points A, B and C.

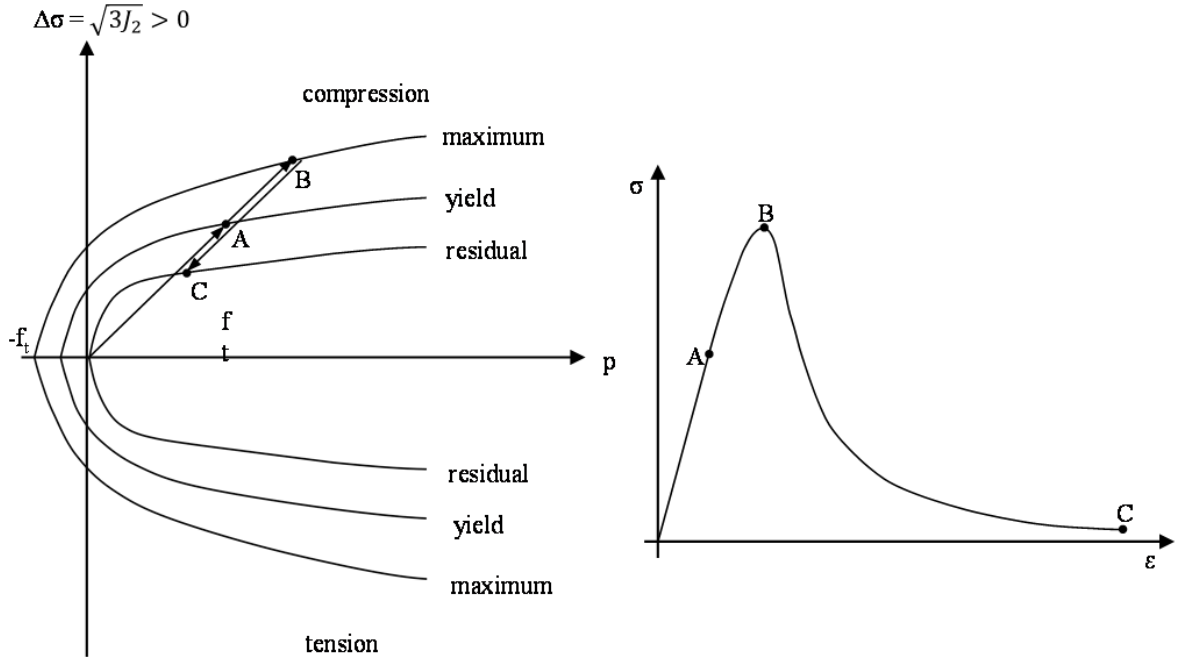

Figure 12 Failure surfaces (left) and uniaxial stress-strain relationship for compression (right) (Markovich et al., 2011; Malvar et al, 1997; Crawford et al., 2012)

In case when enough experimental data for the concrete is not available, the internal parameter generation based only on the unconfined compressive strength and density of concrete gives sufficiently accurate results. This was investigated by Schwer and Malvar, (2005) where a well characterized concrete model of 45.6 MPa unconfined compression strength from the US Army Engineering Research & Development Center (ERDC) was compared with the model based on the KCC internal parameter generator. A good agreement was found between the two models and it was concluded that the K&C concrete material is an excellent material model for modelling the complex behavior of concrete when very little information about the concrete is known.

Strain Rate Enhancement

Strain Rate effects are incorporated in the KCC model using the Dynamic Increase Factor (DIF) that modifies the strength surfaces to represent the changes in strength of the concrete. The DIF can be entered as a curve or defined internally to the KCC model. (Wu et al., 2015)

According to the CEB data (CEB, 1990), the DIF in compression can be formulated as

$$DIF_c = \begin{cases} \left(\frac{\dot{\varepsilon}}{\dot{\varepsilon_s}}\right)^{1.026\alpha} & \dot{\varepsilon} \leq 10^6/s \\ \gamma\left(\frac{\dot{\varepsilon}}{\dot{\varepsilon_s}}\right)^{1/3} & \dot{\varepsilon} > 10^6/s \end{cases} \tag{4.6}$$

where

$$\gamma = 10^{6.156\alpha - 2} \tag{4.7}$$

$$\alpha = \frac{1}{5+0.9f_c'} \tag{4.8}$$

$\dot{\varepsilon}$ is the strain rate; $\dot{\varepsilon_s} = 3 \times 10^{-5}/s$ is the reference strain rate; f_c' is the confined compressive strength in megapascals.

The DIF in tension according to Malvar et al. (Malvar and Crawford 1998; Malvar and Ross 1998) is formulated as

$$DIF_t = \begin{cases} \left(\frac{\dot{\varepsilon}}{\dot{\varepsilon_s}}\right)^{\delta} & \dot{\varepsilon} \leq 1/s \\ \beta\left(\frac{\dot{\varepsilon}}{\dot{\varepsilon_s}}\right)^{1/3} & \dot{\varepsilon} > 1/s \end{cases} \tag{4.9}$$

with

$$\beta = 10^{6\delta - 2} \tag{4.10}$$

$$\delta = \frac{1}{1+0.8f_c'} \tag{4.11}$$

Where the reference strain rate now is $\dot{\varepsilon_s} = 10^{-6}/s$.

4.3. Winfrith Concrete Model – MAT084

The Winfrith concrete model was originally developed in 1980s and was kept in development to meet the requirements by the United Kingdom Nuclear industry. It has been tested against many experiments (Boradhouse, 1995; Broadhouse & Attwood, 1993). The model was used to simulate the experimental impact tests over the reinforced concrete slabs at Heriot-Watt University (Jabbar *et al.*, 2011). It was also used by Izatt *et al.*, (2009) to investigate the effect of impact on the reinforced concrete with and without metal decking. The results were validated by experimental tests. The model was also validated against empirical formulae for cylindrical projectiles.

It has simple input cards and can be used without extensive knowledge of the concrete material. One of the comparatively good feature of this model is that it permits three mutually perpendicular crack planes over an element, which can be visualized in the post processor. (Wu, Crawford and Magallanes, 2012)

The model's stress space is divided into hydrostatic and deviatoric stress state. A normalized volume compaction relation, as shown in Figure 13, characterizes the hydrostatic stress state. Alternatively, a user-defined pressure-volume strain relation can be input using eight pairs of pressure-volume data. (Jabbar *et al.*, 2011)

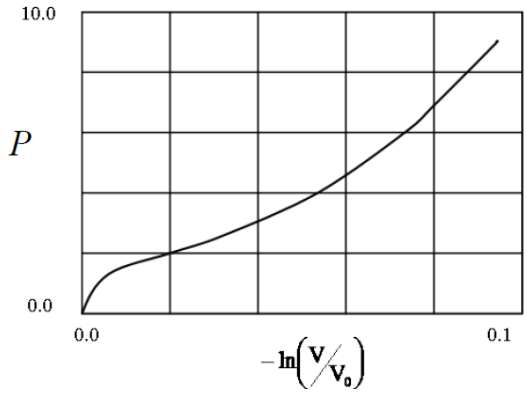

Figure 13 Pressure vs volume strain relationship (Jabbar *et al.*, 2011)

The deviatoric stress state is defined by elastic increments using a local rate-dependent modulus. Its plasticity part or the yield surface is based on the Ottosen Four-Parameter Model (Ottosen, 1977):

$$F(I_1, J_2, cos3\theta) = a\,\frac{J_2}{(f_c')^2} + \lambda\frac{\sqrt{J_2}}{f_c'} + b\frac{I_1}{f_c'} - 1 \tag{4.12}$$

wherein $\lambda = \lambda(cos3\theta)$ and is given as:

$$\lambda = \begin{cases} k_1 \cos[\frac{1}{3}\cos^{-1}(k2\cos 3\theta)] & \cos 3\theta \geq 0 \\ k_1 \cos[\frac{\pi}{3} - \frac{1}{3}\cos^{-1}(-k2\cos 3\theta)] & \cos 3\theta \leq 0 \end{cases} \tag{4.13}$$

and a, b, $k_1$and k_2 are the four parameters and functions of the ratio $\frac{f_t'}{f_c'}$,where f_c' and f_t' are the unconfined compressive strength and unconfined tensile strength respectively. The four tests that are needed to acquire these parameters are uniaxial compression (corresponding to $\theta = 60°$), uniaxial tension ($\theta = 0°$), biaxial compression ($\theta = 0°$), and triaxial compression (($\theta = 60°$) tests.

Strain Rate Enhancement

Strain rate effects are taken into account using strain rate enhancement factors. They, like for KCC model, are based on the recommendation provided by the CEB data (CEB, 1990). However the formulation is different and is implemented in terms of Enhancement factors, which as described by Schwer, (2010) is presented below.

The enhancement factors are formulated based on incremental strains rates. The incremental strain rates are obtained from the incremental strains using the current time step Δt as:

$$\dot{\varepsilon}_{ij} = \frac{\Delta\varepsilon_{ij}^{n}}{\Delta t} \tag{4.14}$$

Effective strain rate $\dot{e}$ is then calculated based on incremental strain rate

$$\dot{\varepsilon}_{vol} = \dot{\varepsilon}_{kk} = \dot{\varepsilon}_{11} + \dot{\varepsilon}_{22} + \dot{\varepsilon}_{33} \tag{4.15}$$

$$\dot{e}_{ij} = \dot{\varepsilon}_{ij} + \dot{\varepsilon}_{kk}\delta_{ij}/3 \tag{4.16}$$

$$\dot{e} = \sqrt{\frac{2}{3}(\dot{e}_{ij}\dot{e}_{ij})} = \sqrt{\frac{2}{3}}\left[\dot{e}_{11}^{2} + \dot{e}_{22}^{2} + \dot{e}_{33}^{2} + 0.5(\dot{e}_{12}^{2} + \dot{e}_{23}^{2} + \dot{e}_{31}^{2})\right] \tag{4.17}$$

The incremental effective strain rate is used to calculate three kind of enhancement factors: tensile modulus, compressive modulus and young's modulus, which is calculated as the average of the former two.

$$E_T = \left(\frac{\dot{e}}{\dot{e}_{0T}}\right)^{1.016\delta} \qquad E_C = \left(\frac{\dot{e}}{\dot{e}_{0C}}\right)^{1.026\alpha} \qquad \dot{e} < 30/s \tag{4.18}$$

$$E_T = \eta\dot{e}^{1/3} \qquad E_C = \gamma\dot{e}^{1/3} \qquad \dot{e} > 30/s \tag{4.19}$$

with

$$\delta = \frac{1}{10 + 0.5f_{cu}} \tag{4.20}$$

$$\alpha = \frac{1}{5 + 0.75f_{cu}} \tag{4.21}$$

$$\log_{10}\eta = 6.933\delta - 0.492 \tag{4.22}$$

$$\log_{10}\gamma = 6.156\alpha - 0.492 \tag{4.23}$$

$$\dot{e}_{0T} = 30 \times 10^{-6}/s \tag{4.24}$$

$$\dot{e}_{0C} = 3 \times 10^{-6}/s \tag{4.25}$$

where $f_{cu}$is the cubic concrete strength in megapascals. The Young's modulus rate enhancement is given as

$$E_E = 0.5\left[\left(\frac{\dot{e}}{\dot{e}_{0T}}\right)^{0.016} + \left(\frac{\dot{e}}{\dot{e}_{0C}}\right)^{0.026}\right] \tag{4.26}$$

The enhancement factor's minimum value is one, which means no rate enhancement or rate effects are considered. Values evaluated less than one are given a value of one.

The following table shows material properties that are enhanced using the factors described above.

Table 1 Material Properties Enhanced as result of Rate Enhancement Factors

Material Property	Rate Enhancement Factor
f_c'	E_C
f_t'	E_T
Young's modulus	E_E
Shear modulus	E_E
Bulk modulus	E_E

4.4. Adopted Concrete Material Model

The concrete model adopted for this study is based on the Concrete Damage Plasticity (CDP) model available in the Abaqus software. It is developed at VTT Technical Research Centre of Finland (Fedoroff, Kuutti and Saarenheimo, 2017). This model enhances the original CDP model in Abaqus to include the confinement dependency in compressive behavior, strain rate dependency in tensile behavior and physically motivated element deletion criteria. In this section, Concrete Damage Plasticity and its various parameters are first explained to provide a review of the original model and then later the enhancements made to the model are discussed.

4.4.1. Concrete Damage Plasticity Model

Concrete damage plasticity (CDP) provides the general capability to model concrete in various types of structures, e.g., beams, shells, trusses and solids. It is a continuum, plasticity-based, damage model for concrete. It is based on isotropic damaged elasticity in combination with isotropic tensile and compressive plasticity to model the inelastic behavior of concrete. It assumes that the two failure mechanisms of concrete are, cracking in tension and crushing in compression. It is mainly intended for the analysis of reinforced concrete structures, though it can be used for the analysis of plain concrete. It is suitable to use for modelling concrete in applications involving monotonic, cyclic and/or dynamic loads with low confining pressures.

CDP is defined in Abaqus by providing four material parameters and defining the inelastic compressive and tensile behavior as a set of pair of points. The inelastic compressive behavior is defined as a stress-strain pairs of points. The tensile behavior, however, additionally can also be defined as stress-fracture energy or stress-cracking displacement relation in the form of point data. The stress-fracture energy or stress-cracking displacement relation has the advantage over

the stress-strain formulation because it diminishes the mesh sensitivity (Hillerborg, Modeer and Pettersson, 1976). The compression and tensile damage can be defined if it is desired to include the effects of degradation of the stiffness.

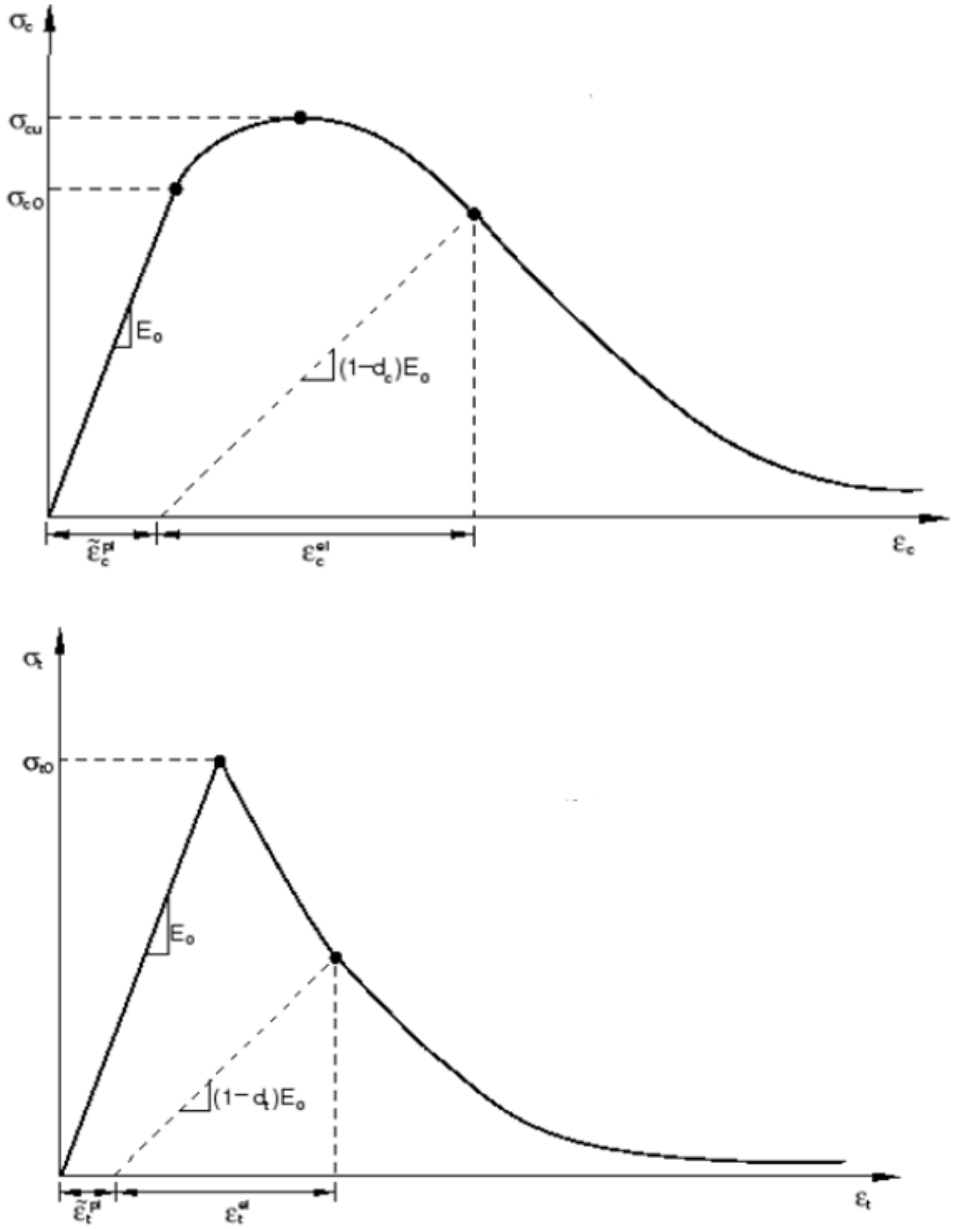

Figure 14 Concrete Response in uniaxial loading in compression (top) and tension (bottom). (Abaqus, Manual)

CDP assumes that the behavior in compression and tension is characterized by the damaged plasticity, e.g. as shown in Figure 14.

Under uniaxial compression the material is assumed to be linearly elastic until the initial yielding at σ_{c0} occurs. Then the material undergoes strain hardening until it reaches the ultimate limit σ_{cu} beyond which it undergoes strain softening. The damage variable d_c, which is assumed to be a function of plastic strains, incorporates the stiffness degradation of the material in the strain-softening region. If the material is unloaded in the strain-softening region, the unloading response becomes weaker and weaker as you go beyond the ultimate stress, because the damage variable d_c accumulates from zero (undamaged material) to maximum value of

one (completely damaged material). ε_c^{el} and $\tilde{\varepsilon}_c^{pl}$ are the elastic and equivalent plastic strains in compression respectively.

In uniaxial tension the stress-strain relation is linear elastic until it reaches the maximum stress σ_{t0}. This failure stress represents the onset of cracking in the material. Beyond this point the material softening occurs representing the formation of micro-cracks. d_t is the damage variable for representing degradation in tensile stiffness. ε_t^{el} and $\tilde{\varepsilon}_t^{pl}$ are the elastic and equivalent plastic strains in tension respectively.

The yield surface of the model is based on yield function of (Lubliner *et al.*, 1989) , and adjustments proposed by (Lee and Fenves, 1998) to take into consideration the difference in evolution of the tensile and compressive strength. In terms of the effective stress space with effective cohesion stress in compression and tension, $\hat{\sigma}_c$ and $\hat{\sigma}_t$ respectively, the yield function can be written as

$$F = \frac{1}{1-\alpha}\left(\sqrt{3J_2(\underline{\hat{\sigma}})} + \alpha I_1\left(\underline{\hat{\sigma}}\right) + \left((1-\alpha)\frac{\hat{\sigma}_c}{\hat{\sigma}_t} - (1+\alpha)\right)\langle\hat{\sigma}_{max}\rangle - \gamma\langle-\hat{\sigma}_{max}\rangle\right) - \hat{\sigma}_c \qquad (4.27)$$

where,

α and γ are the material constants.

$I_1$and $\sqrt{3J_2}$ are the first stress invariant and equivalent Mises stress repectively.

$\hat{\sigma}_{max}$ is the maximum principal effective stress and Macauly bracket notation is given as $\langle x\rangle = \frac{1}{2}(|x| + x)$

CDP uses non-associative flow rule i.e. it does not use the above yield function as the flow potential. The Drucker-Prager hyperbolic function is used as the flow potential, which in terms of current stress tensor $\underline{\sigma}$ is given as:

$$G\left(\underline{\sigma}\right) = \sqrt{\left(ef_{t0}\tan\Psi\right)^2 + 3J_2\left(\underline{\sigma}\right)} + \frac{1}{3}\tan\Psi\, I_1\left(\underline{\sigma}\right) \qquad (4.28)$$

where,

Ψ is the dilation angle, e is the eccentricity and these are the material constants.

f_{t0} is the initial tensile cohesion stress.

It can be noted that in total four material parameters are required to define the yield surface and the flow potential. The CDP model in Abaqus includes a fifth parameter called viscosity parameter that improves the convergence of the solution in the implicit analysis but it is not needed in the Abaqus/Explicit solver. Fedoroff (2017) explains the definitions of the two material parameters α and γ and their effect on the yield surface. (Jankowiak and Lodygowski, 2005) have explained the methods and requirements for the identification of these material parameters. A brief overview of these parameters is presented as follows:

Parameter α

α parameter is dependent on the ratio of the biaxial compressive strength f_{b0} to the uniaxial compressive strength f_{c0} and can be defined as (Jankowiak and Lodygowski, 2005)

$$\alpha = \frac{\left(\frac{f_{b0}}{f_{c0}}\right) - 1}{2\left(\frac{f_{b0}}{f_{c0}}\right) - 1} \tag{4.29}$$

In Abaqus, input is given in the form of $\frac{f_{b0}}{f_{c0}}$ ratio for the calculation of this parameter. The range of typical values of $\frac{f_{b0}}{f_{c0}}$ is from 1.10 to 1.16 giving values of α from 0.08 to 0.12 (Lubliner *et al.*, 1989).

Parameter γ

γ parameter is defined as:

$$\gamma = \frac{3(1 - K_c)}{2K_c - 1} \tag{4.30}$$

where K_c is the ratio of the second stress invariant on the tensile meridian to that on the compression meridian in the Haigh-Westergaard stress space (Abaqus, Manual). The value of K_c is provided as input in the Abaqus for the calculation of this parameter.

Drawing the initial yield surface in the meridian planes shows (Figure 15) the effect of K_c on the shape of the initial yield surface when α is kept constant. It shows that K_c affects the cone

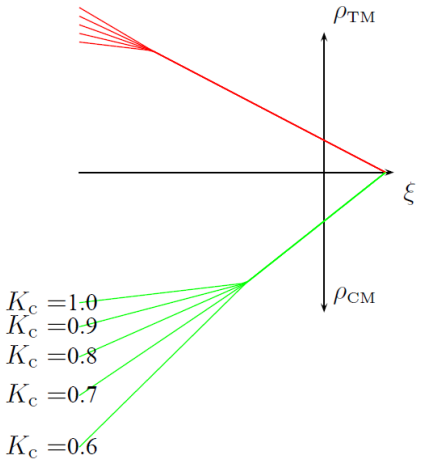

Figure 15 Yield surface dependency on the parameter K_c in meridional view. (Fedoroff, A., 2017).

sharpness (angle of the meridian slope) of the compressive region. Likewise, when viewed in the deviatoric plane, it can be witnessed that in addition to the sharpness of the cone, K_c also

affects the shape of the cone as shown in Figure 16. K_c with a value of 0.5 gives the Rankine Triangle and with a value of 1 gives the Drucker-Prager circle. (Fedoroff, A., 2017).

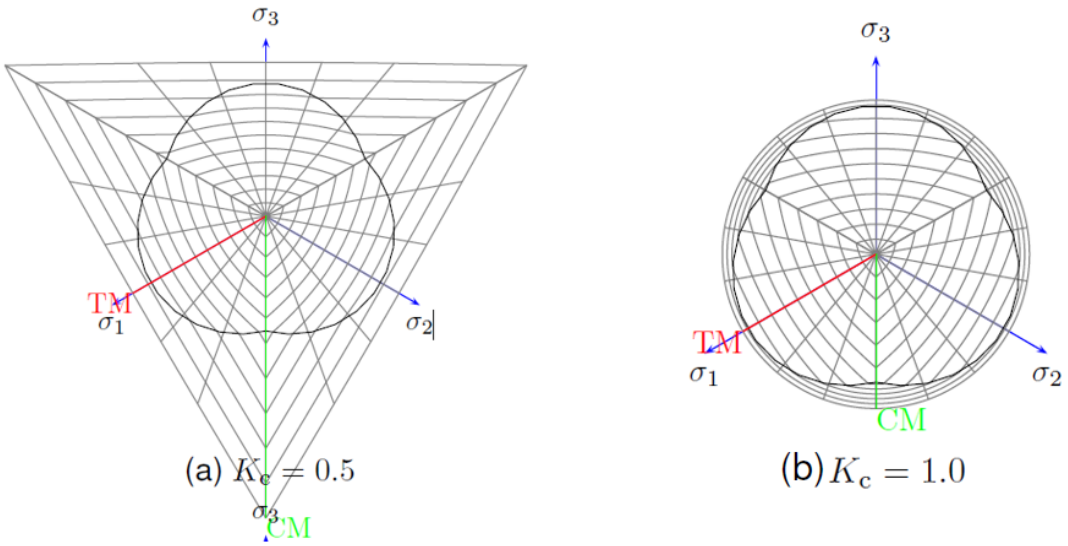

Figure 16 Yield surface dependency on the parameter K_c in deviatoric view. (Fedoroff, A., 2017).

The value K_c may range from 0.5 to 1 but the recommended value is 2/3. (Abaqus Manual).

The Dilation Angle (Ψ)

Dilation angle is the parameter used in the flow potential function. It is the angle of inclination of the failure surface towards the hydrostatic axis when measured in the meridional plane. It is the internal frictional angle of concrete (Kmiecik and Kamiński, 2011) and determines the ratio of plastic volumetric strain increment to the plastic shear strain increment. The dilation angle is shown in Figure 17.

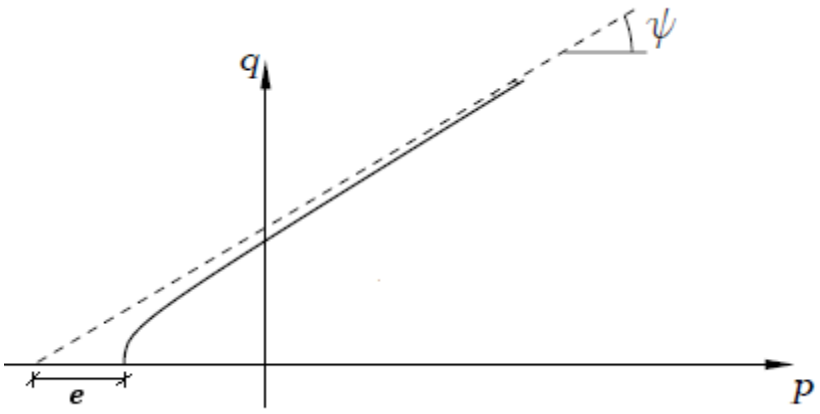

Figure 17 Dilation Angle and Eccentricity in meridional plane for plastic potential function.

Eccentricity (e)

The Drucker-Prager plastic potential function of the CDP model is a hyperbolic function. The eccentricity e is the rate with which this hyperbola of the plastic potential function reaches its asymptote. Mathematically it is the length between the center of hyperbola (the point of intersection of the asymptotes of the hyperbola) and its vertex when measured along the hydrostatic axis. When $e = 0$, the meridian plane is necessarily a straight line (Classic Drucker-Prager criteria). It has been observed in the experiments that the meridian is a curve and not a straight line. (Kmiecik and Kamiński, 2011)

4.4.2. Modified Concrete Damage Plasticity model

Introduction

As was discussed in Section 4.1, concrete is a strain rate dependent material, i.e., its strength increases when it is dynamically loaded in both compression and tension. The VTT Model customizes the original CDP model to include the strain rate effects in compression and tension, and a physically motivated element deletion criterion to successfully capture the macroscopic concrete fracture. The modification is applied to the original CDP model by means of an Abaqus VUSDFLD user subroutine.

The increase in compressive strength has been attributed to the confinement due to the inertial effects (Li and Meng, 2003). Such conclusions are derived from Split-Hopkinson pressure bar (SHPB) tests. Similarly Hopkinson's tests and simulations by Grote, Park and Zhou, (2001) and Park, Xia and Zhou, (2001) have reached towards the same conclusions.

The physical reason behind the dynamic increase in tensile strength is subject to many discussions. The observations of the Klepaczko and Brara, (2001) in SHPB tests for tensile strength shows that failure surface of spalling slices through the aggregates which are lying embedded inside concrete. This is distinct from the quasi-static tensile tests where the failure surface does not cut through the aggregates and they are staying intact. "*Hence, it has been proposed, (Ross;Jerome;Tedesco;& Hughes, 1996) and (Min;Yao;& Jiang, 2014), that at slow strain rates the cracks in the concrete matrix grow around the aggregates, whereas at high strain rates the cracks propagate directly through the aggregates. Hence, depending on the type and size of aggregates, the peak stress and fracture energy increase as the strain rate increases.* (Fedoroff, Kuutti and Saarenheimo, 2017)*"*

Element Deletion

One of the important issues of the publications in the impact simulations is the element deletion. In high speed impact simulations, techniques like XFEM and adaptive re-meshing are very costly to implement and therefore to include the macroscopic crack initiation and propagation, spalling , scabbing and punch cone formation in a cost-effective way, it is important to include a physically motivated element deletion criteria. (Fedoroff, Kuutti and Saarenheimo, 2017)

A cut-off value of equivalent plastic strain in compression of 0.2 is chosen as an element deletion criteria by Rodríguez, Martínez and Martí, (2013) for simulating the impact of missile on reinforced concrete targets. The choice of this value for element deletion criteria is purely based on numerical reasons since if an element deforms excessively then the explicit central difference time integration in Abaqus fails. Ågårdh and Laine, (1999), however, chose a

deletion criteria that was not utilized primarily because of the numerical stability. He chose a criterion where the cut-off value of equivalent strain depended on the confining pressure. This is a more physically rational approach as the elements in highly confined zones are not deleted at the same strain as in the low confined regions.

"Our position on the element deletion criterion is that it should be first of all physically based, in other words a cracked element should be removed if its load bearing capacity is lost. In addition to this physical criterion, one should add a criterion that serves computational purposes so that the hard missile impact simulation can be run without numerical errors." (Fedoroff, Kuutti and Saarenheimo, 2017)

Description Of The model

The original CDP model in Abaqus as explained couples elastic-damage and elastic-plastic behavior but this model excludes the damage and includes only elasticity and plasticity.

The yield surface and the flow potential. The yield surface and the flow potential necessarily remains the same as described is Section 4.4.1. Yield surface without the damage in the current stress space $\underline{\underline{\sigma}}$ however modifies as

$$F\left(\underline{\underline{\sigma}}, f_c, f_t\right) = \frac{1}{1-\alpha}\left(\sqrt{3J_2(\underline{\underline{\sigma}})} + \alpha I_1\left(\underline{\underline{\sigma}}\right) + \left((1-\alpha)\frac{f_c}{f_t} - (1+\alpha)\right)\langle\sigma_{max}\rangle - \gamma\langle-\sigma_{max}\rangle\right) - f_c \quad (4.31)$$

In a general triaxial stress state, the cohesive stress in compression, $f_c(\varepsilon_c^p)$, and in tension , $f_t(\varepsilon_t^p)$, are assumed to evolve with changing equivalent plastic strains representing the evolution of the yield surface. The equivalent plastic strains are defined in terms of the minimum and maximum principal strain increments as

$$\dot{\varepsilon}_c^p = -\left(1 - r\left(\underline{\underline{\sigma}}\right)\right)\dot{\varepsilon}_{min} \quad (4.32)$$

$$\dot{\varepsilon}_t^p = r\left(\underline{\underline{\sigma}}\right)\dot{\varepsilon}_{max} \quad (4.33)$$

where $r\left(\underline{\underline{\sigma}}\right)$ is the weight coefficient. Its values 1, 0.5 and 0 correspond to the uniaxial tension, pure shear and uniaxial compression respectively.

Hardening/Softening behavior in compression. This section explains the formulations that are used to develop the concrete softening/hardening relation in compression for concrete that includes the confinement dependency. Consider $\underline{\underline{\sigma}} = diag(-\sigma_{cnf}, -\sigma_{cnf}, -\sigma_{axi})$, a "confined uniaxial" stress state, where, σ_{cnf} and σ_{axi} represent the confining pressure and axial stress, respectively. For this state of stress, the yield condition from equation (4.31) becomes

$$\sigma_{axi} \leq \frac{1 + 2\,\alpha + \gamma}{1 - \alpha}\sigma_{cnf} + f_c \quad (4.34)$$

The elastic constitutive relations in combination with the additive breakdown of the small strains into elastic and plastic parts yield the following expression for the equivalent plastic

strain in compression , ε_c^p, in terms of the axial total strain, ε_{axi}^{tot}, and the axial and confinement stresses.

$$\varepsilon_c^p = \varepsilon_{axi}^{tot} - \frac{\sigma_{axi} - 2\nu\,\sigma_{cnf}}{E} \tag{4.35}$$

where E is the elastic modulus and ν is the Poisson's ratio. Equations (4.34) and (4.35) are true particularly in the case of peak values of the axial stress, $\sigma_{axi,peak}(\sigma_{cnf})$ and the respective total strain $\varepsilon_{axi,peak}^{tot}(\sigma_{cnf})$. As the confinement dependency needs to be introduced in compression, both these values are assumed dependent on the confinement stress. The peak values for the cohesive stress and plastic strain are obtained from Equations (4.34) and (4.35), repectively, as given below.

$$f_{c,peak}(\sigma_{cnf}) = \sigma_{axi,peak}(\sigma_{cnf}) - \frac{1+2\alpha+\gamma}{1-\alpha}\sigma_{cnf} \tag{4.36}$$

$$\varepsilon_{c,peak}^{p}(\sigma_{cnf}) = \varepsilon_{axi,peak}^{tot}(\sigma_{cnf}) - \frac{\sigma_{axi,peak}(\sigma_{cnf}) - 2\nu\,\sigma_{cnf}}{E}$$

The confinement dependency is introduced based on the relation defined in Eurocode (Bamforth, Chisholm, Gibbs, and Harrison, 2008), as follows.

$$\sigma_{axi,peak}(\sigma_{cnf})/\sigma_{axi,peak}(0) = \begin{cases} 1.0 + 5.0 \times \sigma_{cnf}/\sigma_{axi,peak}(0)\,, \sigma_{cnf}/\sigma_{axi,peak}(0) \le 0.05 \\ 1.125 + 2.5 \times \sigma_{cnf}/\sigma_{axi,peak}(0)\,, \sigma_{cnf}/\sigma_{axi,peak}(0) \ge 0.05 \end{cases}$$

$$\varepsilon_{axi,peak}^{tot}(\sigma_{cnf})/\varepsilon_{axi,peak}^{tot}(0) = (\sigma_{axi,peak}(\sigma_{cnf})/\sigma_{axi,peak}(0))^2 \tag{4.37}$$

where the confinement stress is evaluated as

$$\sigma_{cnf}(t) = 0.2\langle -\sigma_{max}(t)\rangle + 0.8\; max\,\langle -\sigma_{max}(t)\rangle \tag{4.38}$$

In a triaxial stress state, $\langle -\sigma_{max}(t)\rangle$ is the current maximum principal stress and $max\,\langle -\sigma_{max}(t)\rangle$ is the largest maximum principal stress ever.

The evolution of the cohesive stress with the plastic strain as suggested by (Lee and Fenves, 1998) can be written with confinement dependency as:

$$f_c(\varepsilon_c^p, \sigma_{cnf}) = f_{c0}\left(\left(1 + a_c(\,\sigma_{cnf})\right)\exp\left(-b_c(\sigma_{cnf})\varepsilon_c^p\right) - a_c(\sigma_{cnf})\exp(-2b_c(\sigma_{cnf})\varepsilon_c^p)\right) \tag{4.39}$$

where f_{c0} is the initial yield stress and $a_c(\,\sigma_{cnf})$ and $b_c(\sigma_{cnf})$ are coefficients defined below.

$$a_c(\,\sigma_{cnf}) = 2\frac{f_{c,peak}(\sigma_{cnf})}{f_{c0}} + 2\sqrt{\left(\frac{f_{c,peak}(\sigma_{cnf})}{f_{c0}}\right)^2 - \frac{f_{c,peak}(\sigma_{cnf})}{f_{c0}} - 1} \tag{4.40}$$

$$b_c(\,\sigma_{cnf}) = -\frac{1}{\varepsilon_{c,peak}^{p}(\sigma_{cnf})}\ln\left(\frac{1 + a_c(\,\sigma_{cnf})}{2a_c(\,\sigma_{cnf})}\right)$$

For material contants $\alpha = 0.12$ and $\gamma = 1.5$, and concrete grade C50/60, the evolution of the cohesive stress in terms of plastic strain is shown in Figure 18 for various confinement stresses.

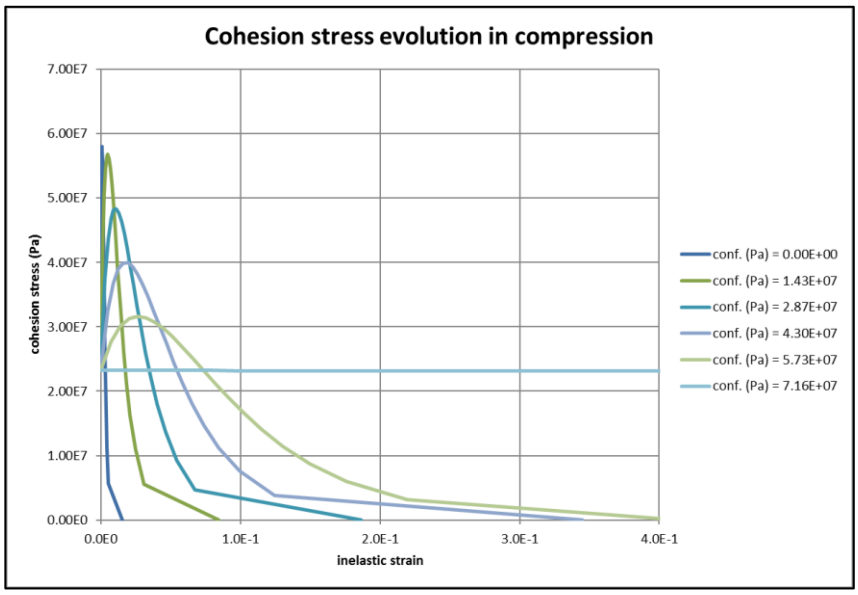

Figure 18 Evolution of the cohesion stress in compression

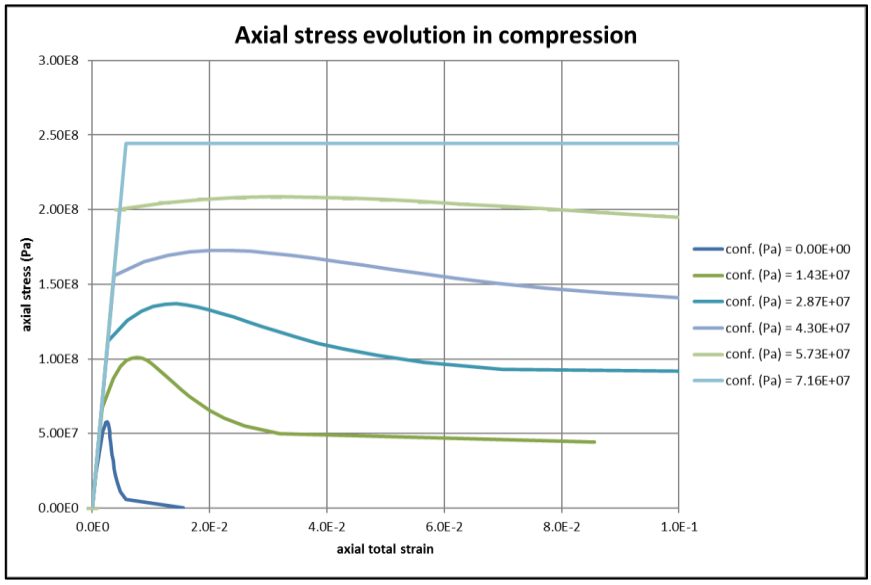

Figure 19 Evolution of the axial stress in compression

Similarly, the evolution of the axial stress in terms of total strain for various confinement stresses is shown in Figure 19.

Softening behavior in tension. For a uniaxial tensile stress state $\underline{\sigma} = diag(\sigma_{axi}, 0, 0)$, the yield equation becomes

$$\sigma_{axi} \leq f_t \tag{4.41}$$

where σ_{axi} is the axial tensile stress. By using the elastic constitutive relations and decomposition of small strains into elastic and plastic shares, we obtain the equation for equivalent plastic strain in tension, ε_c^p, as follows:

$$\varepsilon_t^p = \varepsilon_{axi}^{tot} + \frac{\sigma_{axi}}{E} \tag{4.42}$$

Based on the exponential evolution relation of the cohesive stress in tension as proposed in (Lee and Fenves, 1998), the cohesive stress in tension can be written as

$$f_t\left(\varepsilon_t^p, \dot{\varepsilon}_{max}^{tot}\right) = f_{t0}(\dot{\varepsilon}_{max}^{tot}) \exp\left(-\frac{f_{t0}(\dot{\varepsilon}_{max}^{tot}) l_{ch}}{G_f(\dot{\varepsilon}_{max}^{tot})} \varepsilon_t^p\right) \tag{4.43}$$

Where $\dot{\varepsilon}_{max}^{tot}$ is the maximum principal strain rate and $G_f(\dot{\varepsilon}_{max}^{tot})$ is the fracture energy. The strain rate is computed in the same principal as the confinement stress, i.e., in the model it is a linear combination of the current strain rate and highest ever strain rate. The peak stress $f_{t0}(\dot{\varepsilon}_{max}^{tot})$ and the fracture energy $G_f(\dot{\varepsilon}_{max}^{tot})$ are both strain rate dependent and are increased using a dynamic increase factor for each. The dynamic increase factor relation for the peak stress is chosen based on the suggestions given in (fib, 2010) whereas for fracture energy it is based on the (Weerheijm and Vegt, 2010). Each relation is as a bilinear relation on a logarithmic scale of strain rates as shown in Figure 20.The evolution of the cohesive stresses in tension for different strain rates is shown in Figure 21 and the axial stress evolution in tension is shown in Figure 22.

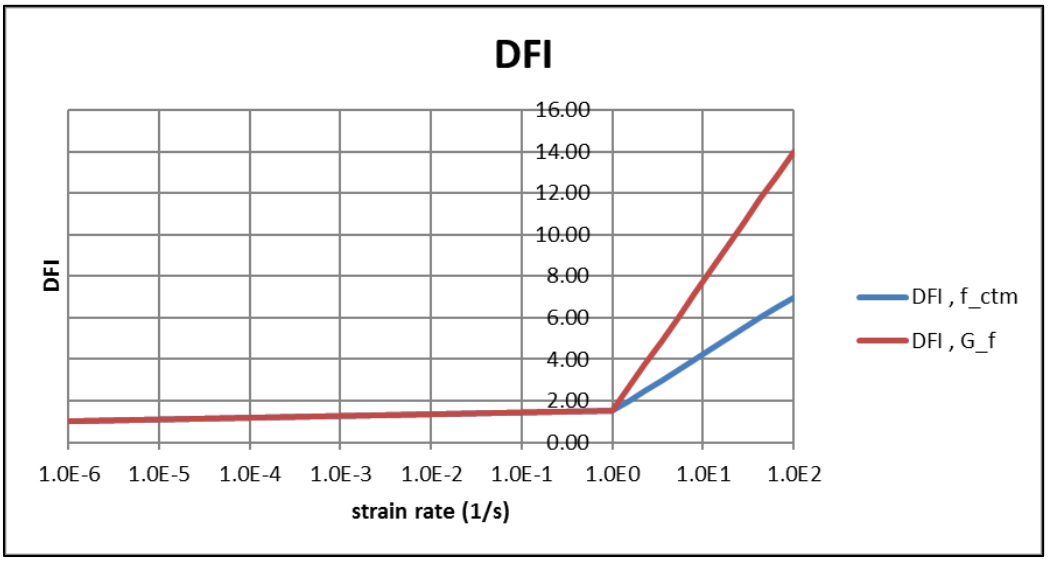

Figure 20 Dynamic Increase factor for peak stress in tension and fracture energy.

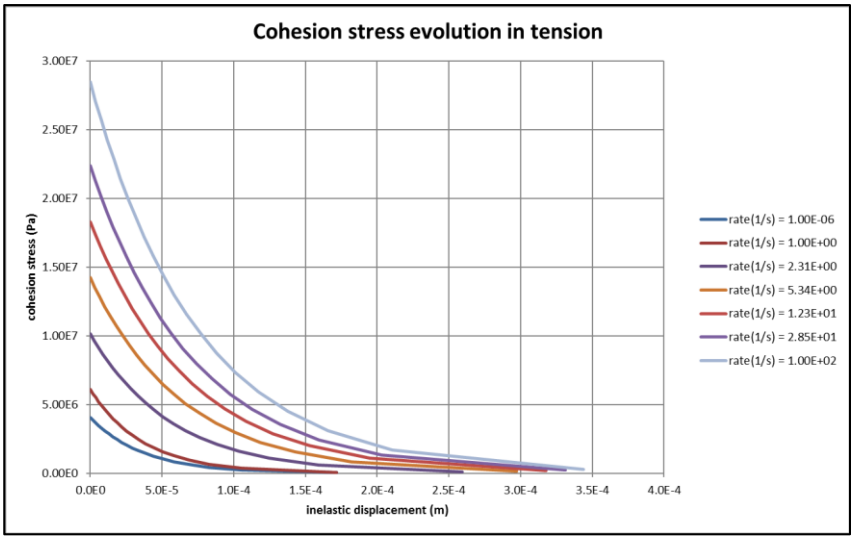

Figure 21 Evolution of the cohesion stress in tension

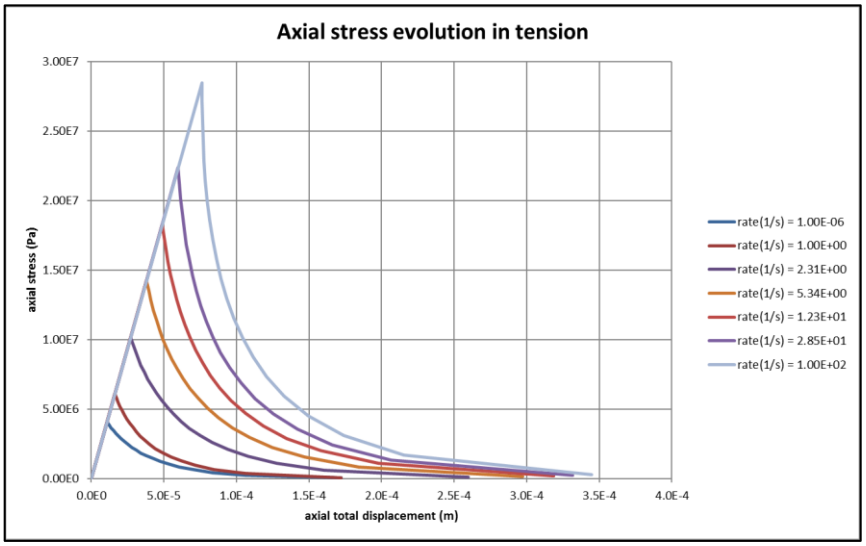

Figure 22 Evolution of the axial stress in tension

Element deletion criteria. The final inelastic strain value varies with varying confinement stresses as seen in Figure 18. Similarly, the ultimate values of inelastic displacement in Figure 21 are changing with the varying strain rates. This clearly suggest that the cutoff values for the element deletion thus needs to be dependent on the confinement stress in compression and the strain rate in tension. Despite different confinement stresses and strain rates, it is observed that in both cases, the cohesive stress is reaching zero asymptotically. Therefore, a small threshold value of the cohesive stress can be used for obtaining the cutoff values of plastic strains from equation (4.39) and (4.43) in compression and tension respectively. The choice of threshold value of the cohesive stress is $1Pa$, which is small enough for the element that it has dissipated 99.99% of its energy before being deleted. Figure 23 and Figure 24 show the cutoff values of the inelastic strain in compression and cracking displacement in tension respectively.

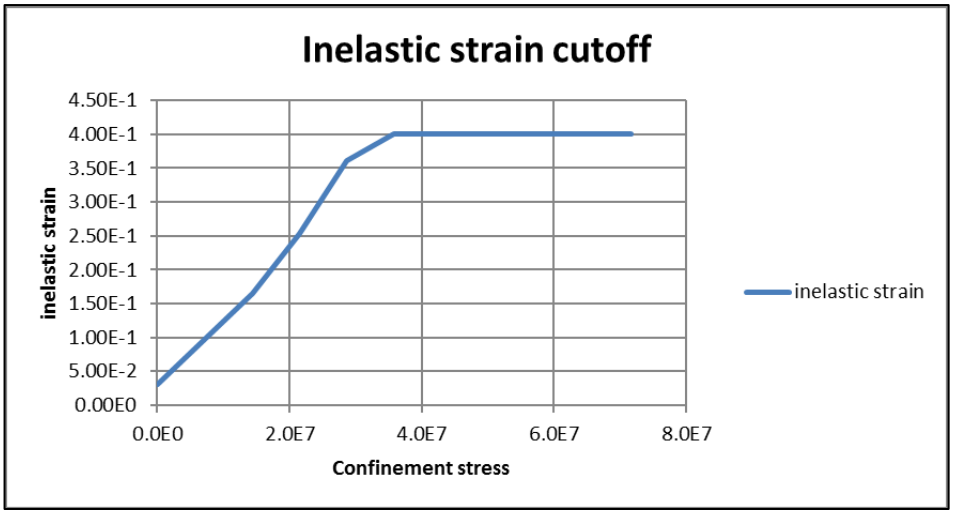

Figure 23 Cutoff values for inelastic strain in compression.

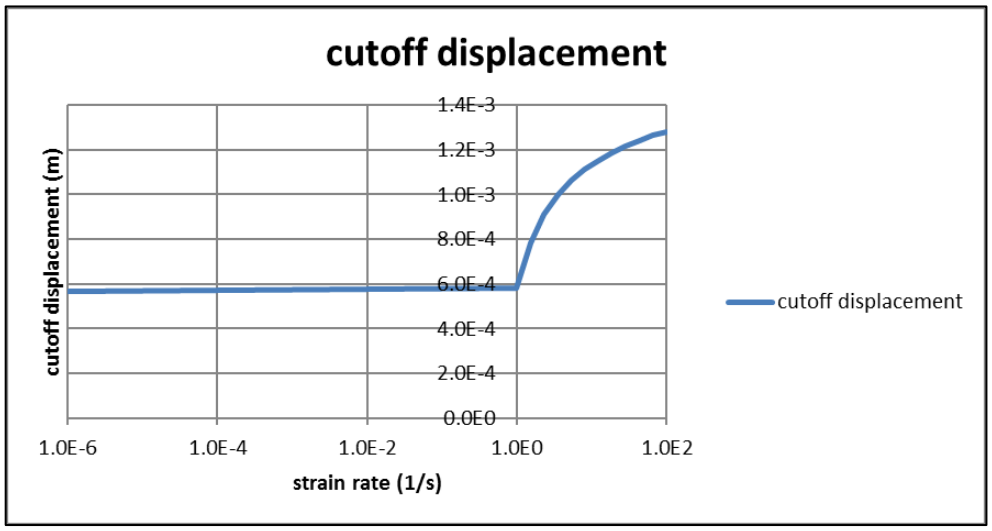

Figure 24 Cutoff values for cracking displacement in tension.

Note that the inelastic strain in compression is bounded by a maximum cutoff value of 0.4 since a value greater than this would lead to excessive distortion of the elements such that the explicit time integration scheme would fail at some instance during the simulation.

Implementation in Abaqus

The above model is implemented in Abaqus using the VUSDFLD user subroutine. Initially, for a particular grade of concrete, the cohesive stress evolution curves in compression for a range of confinement stresses are input in the CDP model in Abaqus as compressive behavior. The different confinement stresses are input in field variable. Similarly, the cohesive evolution in tension for various strain rates is input in the CDP model as tensile behavior. The strain rates are input as another field variable. Using the formulations of the model, VUSDFLD subroutine is used to calculate the current confinement stress and current strain rate at a material point as redefined field variables. The defined values in the compressive behavior and tensile behavior are then interpolated for the redefined field variables of confinement stress and strain rate.

The element deletion criteria is defined using a solution-dependent state variable in the same subroutine. It acts as a flag for the element deletion. Once an element deletion criteria is reached based on the above model, the state variable is given a value of zero. That means the element

is deleted and is no longer able to carry stresses and have no contribution to the stiffness of the model.

4.5. Material Model for Reinforcement

The material model for reinforcement is an elastic-plastic model including progressive damage. A schematic diagram of such a model is shown in Figure 25.

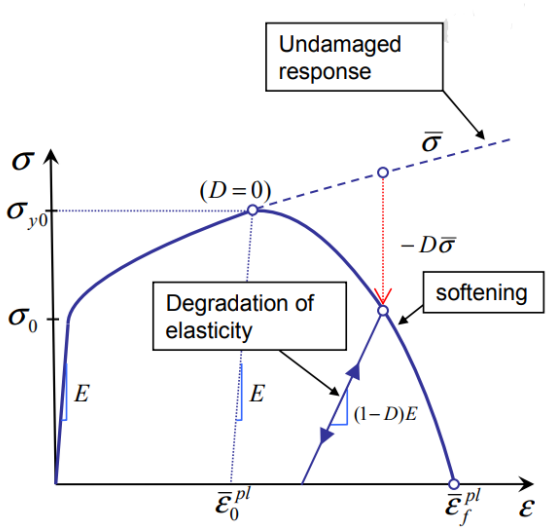

Figure 25 Elastic-Plastic Model with progressive damage. (Abaqus, Manual)

The Figure shows that the material exhibits an elastic-plastic response until it reaches damage initiation criteria $\bar{\varepsilon}_0^{pl}$ beyond which the material undergoes accumulating damage. The damage manifests itself as softening of the yield stress and/or degradation of the elasticity. The overall damage variable D captures the active damage mechanisms and it accumulates from zero (no damage) to a value of one, which indicates a fracture (Abaqus, Manual).

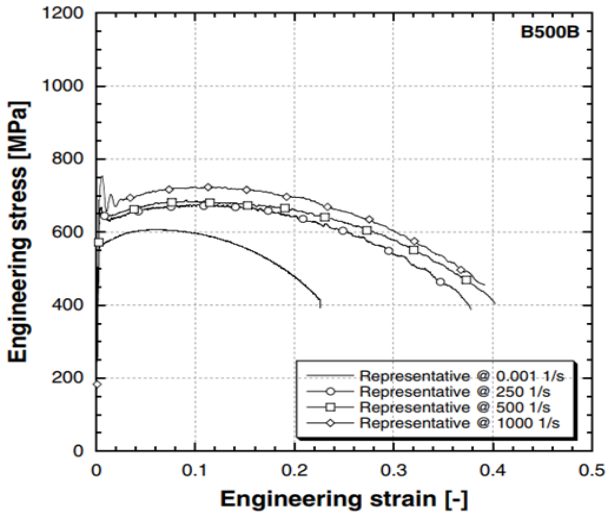

Figure 26 Experimental stress-strain data for B500B reinforcement steel bar

The model was used in simulating the reinforcement behavior in IRIS P1 benchmark test (Fedoroff, Kuutti and Saarenheimo, 2017). It is calibrated based on the experimental results

of Cadoni and Forni, (2015) who tested specimens of B500A, B500B and B500C reinforcement steel in tension for a wide range of strain rates. The stress-strain relation for B500B reinforcement steel bar from the experiments is shown in Figure 26.

The plasticity of the material is incorporated by using the Mises yield surface with isotropic hardening/softening. The isotropic hardening means that the yield surface flows uniformly in every direction. The hardening and softening of the material is parabolic in shape and is strain rate dependent. The strain rate dependency makes the model more suitable for impact analysis as compared to the normal bilinear models used for reinforcement.

The Johnson-Cook damage criterion is used to model the progressive ductile damage of the reinforcement. It is a strain rate dependent damage criterion. The Johnson-Cook damage initiation criteria defines the equivalent plastic strain $\bar{\varepsilon}_D^{pl}$ at the onset of damage as:

$$\bar{\varepsilon}_D^{pl} = [d_1 + d_2 \exp(-d_3\eta)]\left[1 + d_4 \ln\left(\frac{\dot{\bar{\varepsilon}}^{pl}}{\dot{\varepsilon}_0}\right)\right](1 + d_5\hat{\theta}) \tag{4.44}$$

where $d_1, \ldots, d_5$ are the failure parameters, $\dot{\bar{\varepsilon}}^{pl}$ is the equivalent plastic strain rate, $\dot{\varepsilon}_0$ is the reference strain and $\hat{\theta}$ is the non-dimensional temperature.

The damage evolution defines the post-damage initiation behavior of the material. The damage evolution is defined using fracture energy and a linear softening of the stress-strain response. The element is deleted when the damage value reaches a value of 1. The stress-strain behavior of the reinforcement modelled on the above settings with and an initial yield strength 520MPa and ultimate tensile strength of 680MPa is shown in Figure 27.

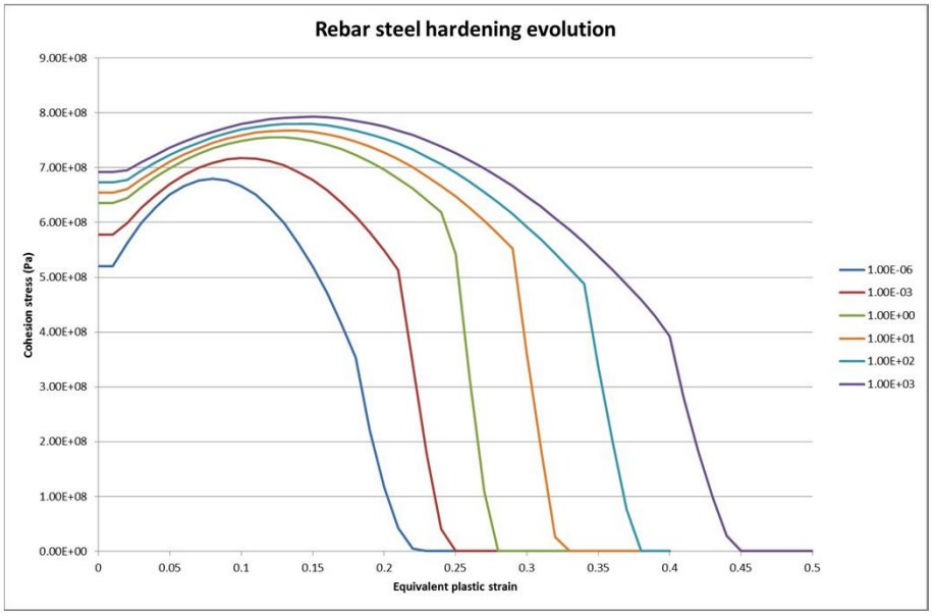

Figure 27 Reinforcement steel material model for reinforcement with 520MPa initial yield stress.

5. VALIDATION STUDY

5.1. Introduction

The customized concrete damage plasticity model is originally developed keeping in view the high-speed velocity impacts. It has been validated in simulating IRIS P1 benchmark test (Fedoroff, Kuutti and Saarenheimo, 2017). In the test, a 168 mm diameter hard missile with a mass of 47.4 kg hits a 2 m by 2 m reinforced concrete slab with an initial velocity of 136 m/sec and punches through the slab. The thickness of the slab is 250 mm. More details about the experiment can be obtained from (Vepsä, Saarenheimo, Tarallo, Rambach, and Orbovic, 2012).The model qualitatively agreed with many aspects of experimental observations such as the formation of confinement zone in front of the missile and element deletion at the boundary of the confinement zone. The displacements were claimed to be in good quantitative agreement with the test. The punch cone formed in the simulation had a narrower angle than the one found in experiment. The missile tail speed in the experiment was 34 m/s whereas in the simulation it was tending to about 40 m/s.

Since this study deals with low-velocity impacts it was considered to check the capability of the model in simulating the low-velocity impact tests as the construction industry scenarios typically include lower velocities and higher masses. The experimental tests carried out at Heriot-Watt University (Izatt *et al.*, 2009) were chosen for this validation study. This chapter contains the details about the experimental tests and the finite element analysis of these tests.

5.2. Description of Tests

The experimental program included five impact tests of an I-sections with concrete slabs. The velocity of the impact was low and so more relevant to the construction industry. Three of those tests included reinforced concrete slabs as targets whereas the remaining two had the plain concrete slabs. For this validation study, the three tests with the reinforced concrete slabs are chosen.

All the slabs were 760 mm square and 78 mm thick. The reinforcement mesh was 6 mm deformed bars provided at 75 mm spacing only near the bottom of the slab. The cover to the bottom surface of the concrete was 15 mm. The compressive strength of concrete was 43.4 MPa (150 mm cube) and its tensile splitting strength was 1.91 MPa. The reinforcement had a yield strength of 549 MPa and an ultimate strength of 618 MPa. All the slabs were restrained with the help channel section at all edges and large bolts at four corners.

The impactor was a 102×64 I-Section (Rolled steel joist) which had a heavy mass connected on top of it. The total weight of the impactor (I-section and the heavy mass) was 198 kg.

Test Results

Table 2 includes the information about three tests considered for this validation study. In the first two tests, the I-section perforated through the slab whereas in the third test it penetrated into the slab but did not perforate. Figure 28 shows the I-section perforated through the slab S1 that had the impactor dropped on it from 2.5 m. Figure 29 shows the lower (distal face) of the slab S3.

Table 2: Details of tests

Slab/Test No.	*Drop Height (m)*	Failure Type
S1	2.50	Perforated
S2	1.5	Perforated
S3	0.75	Penetrated but not perforated

Figure 28 Perforation of the I-section in Slab S1 (Izatt *et al.*, 2009)

Figure 29 Distal face of the Slab S3 (No perforation) (Izatt *et al.*, 2009)

The acceleration was recorded at the slab and the impactor using the accelerometer. The velocities of the impactor for various impacts (including the two that are not analyzed in this study) are shown in Figure 30, which were generated by integrating the acceleration data. The

sudden change huge change in velocity for some tests past around 0.05 sec indicates a rebound. This rebound is resulted from the second impact of the heavy mass on top of the I-section when the I-section has completely perforated through the slab. This is not a critical aspect of our investigation as the interest is in the that range of time in which the I-section hits and perforates through the slab.

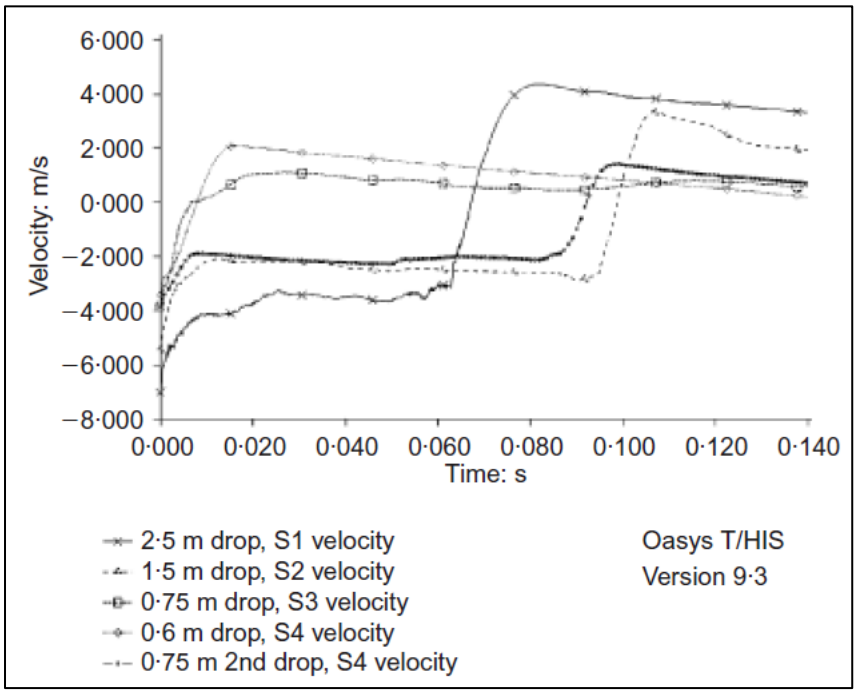

Figure 30 Velocity of impactor various tests. (Izatt *et al.*, 2009)

5.3. Numerical Modeling

Abaqus/Explicit solver is used to analyze slabs S1, S2 and S3 numerically. A three-dimensional model has been used to model the slab using the Langrangian formulation. The concrete slab has been discretized with eight-node hexahedron elements C3D8R. An aspect ratio close to one is maintained for all the elements during discretization. The C3D8R is a reduced integration element and default hourglass control formulations are used to control the hourglass modes.

The impactor is modelled as a three dimensional body with the material properties of steel. It has a density of 7850 kg/m^3, elastic modulus of 210 GPa and a Poison's ratio of 0.3. Rigid body constraints are applied to the elements of the impactor to assign rigid behavior to the elements. This choice is based on the fact that the steel is very stiff as compared to the concrete. When treated as rigid, the solver ignores these elements in the calculations and no storage is assigned for the history variable. As a result, the simulation is made more cost efficient. The impactor consists of an I-section and a heavy mass on top of it as shown in Figure 31. The dimensions of the square heavy mass were chosen so that based on the density of steel, mass of the impactor is same as in the experiment. The impactor was assigned an initial velocity field related to the height of the drop weight for various tests. The penalty constraint formulation is used for contact constraint enforcement. Contact was modelled between the impactor and the exterior top surface of the slab. Since the material model involves element deletion, internal surfaces were also included in the contact domain in case when exterior

surface will erode as a result of penetration of the impactor. The contact in the normal direction was modelled as “Hard Contact” and in the tangential direction was modelled with stiffness coefficient of 0.6 for concrete-to-concrete interface and 0.5 for steel (impactor)-to-concrete interface. These coefficients were taken based on the study by (Fedoroff, Kuutti and Saarenheimo, 2017).

The reinforcement bars were discretized with 2 node beam elements. A full bond between the reinforcement bars and concrete was achieved by modelling the reinforcement as embedded in the concrete. For simplicity, the boundary conditions were modelled as fully restrained on all sides. The model of the concrete slab and reinforcement is shown in Figure 32.

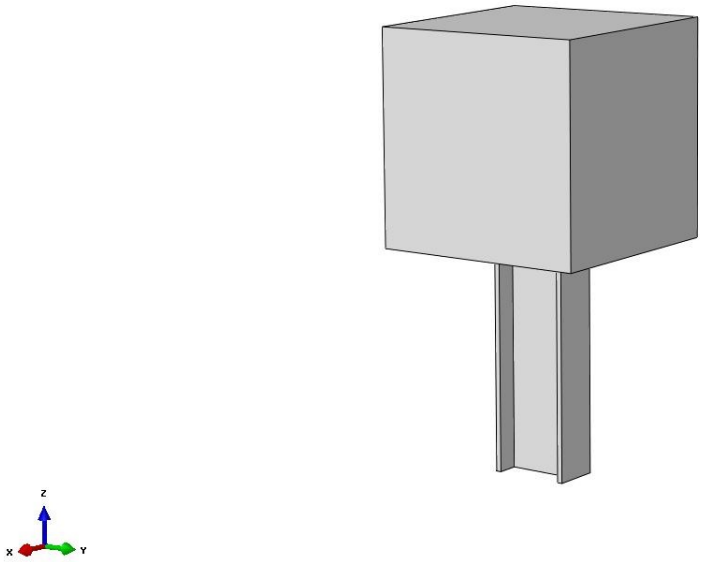

Figure 31 Model of Impactor consisting of an I-section and a heavy mass attached on top of it.

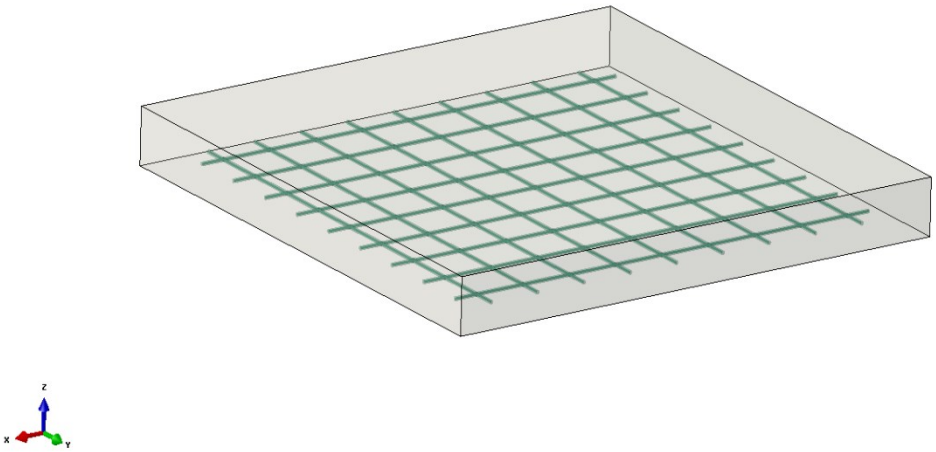

Figure 32 Model of concrete slab and reinforcement mesh.

The modified CDP model is used as a material model for concrete. The values of the four material parameters that are the required for the CDP model as were discussed in Section 4.4.1 are given in Table 3. Material properties for the concrete are given in Table 4.

Table 3 Concrete Damage Plasticity Model Parameters

Dilation Angle	**Eccentricity**	f_{b0}/f_{c0}	K_c
30	0.01	1.15	0.75

Table 4 Material Properties of concrete

Density (kg/m^3)	2500
Compressive strength (MPa)	34.7 (Equivalent to cubic 43.4 MPa in experiment)
Tensile Strength (MPa)	1.9
Poisson's ratio, ν	0.22
Elastic Modulus (GPa)	31.5

The inelastic behavior of concrete in compression and tension for these material properties is as shown in Figure 33 and Figure 34 respectively. These behaviors are input as point data into the Abaqus.

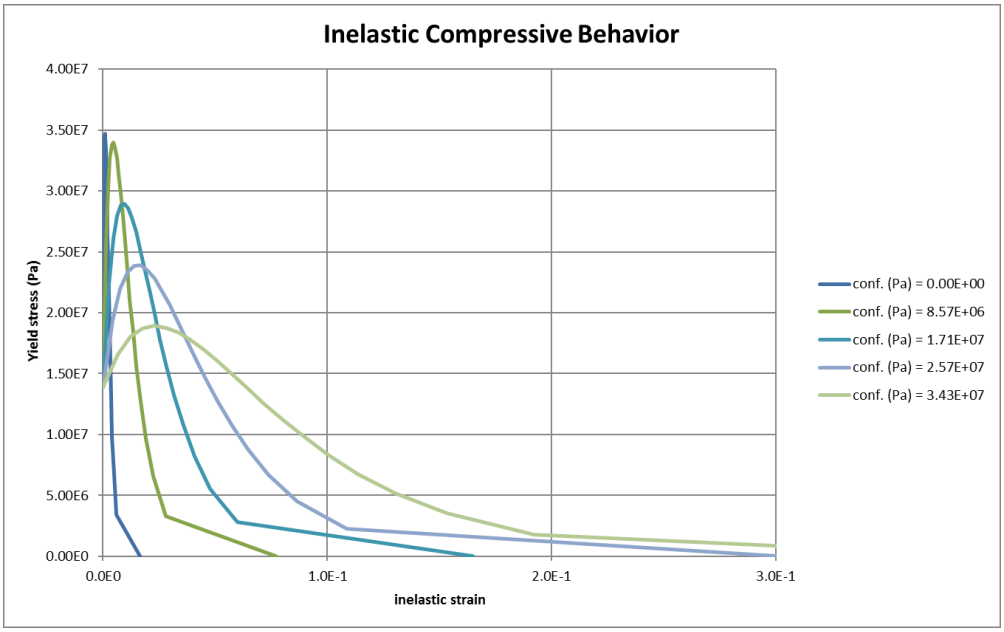

Figure 33 Inelastic Compressive behavior of concrete evolving with confinement stresses.

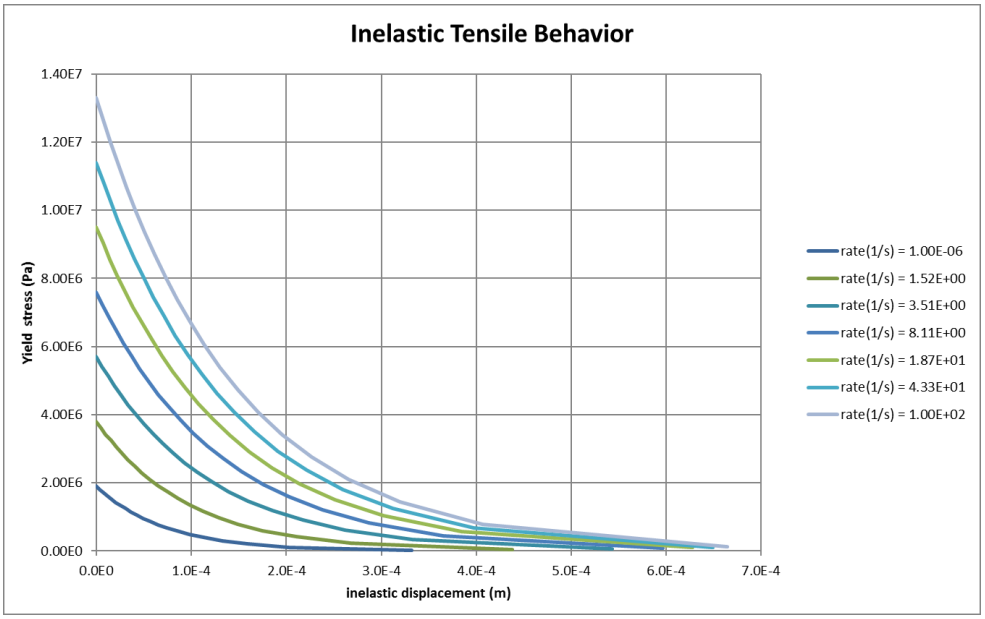

Figure 34 Inelastic Tensile behavior evolving with different strain rates

The reinforcement is modelled as based on the model explained in Section 4.5. The material properties of the reinforcement steel are given in Table 5. The strain-rate dependent hardening/softening behavior is input as point data using the Mises plasticity. The Johnson-cook damage initiation criteria is defined using the material failure parameters given in Table 6. With these failure parameters, in quasi-static rate settings, the damage is initiated at 18% of the equivalent plastic strain. Damage evolution is defined based on the fracture energy of 0.8MN-m at Quasi-static rate. Past the damage initiation criteria, the material linearly softens until it is fully degraded and deleted eventually. The whole stress-strain behavior of reinforcement with the given material properties and the material failure parameters is shown at various rates in Figure 35.

Table 5 Material Properties of Reinforcement Steel

Density (kg/m^3)	7850
Yield Strength (MPa)	549
Ultimate tensile strength (MPa)	618
Poisson's ratio, ν	0.3
Elastic Modulus(GPa)	210

Table 6: Parameters for Johnson-Cook Damage Initiation Criteria

d1	d2	d3	d4	d5	Reference Strain Rate
0.18	0	0	0.02	0	1×10^{-6}

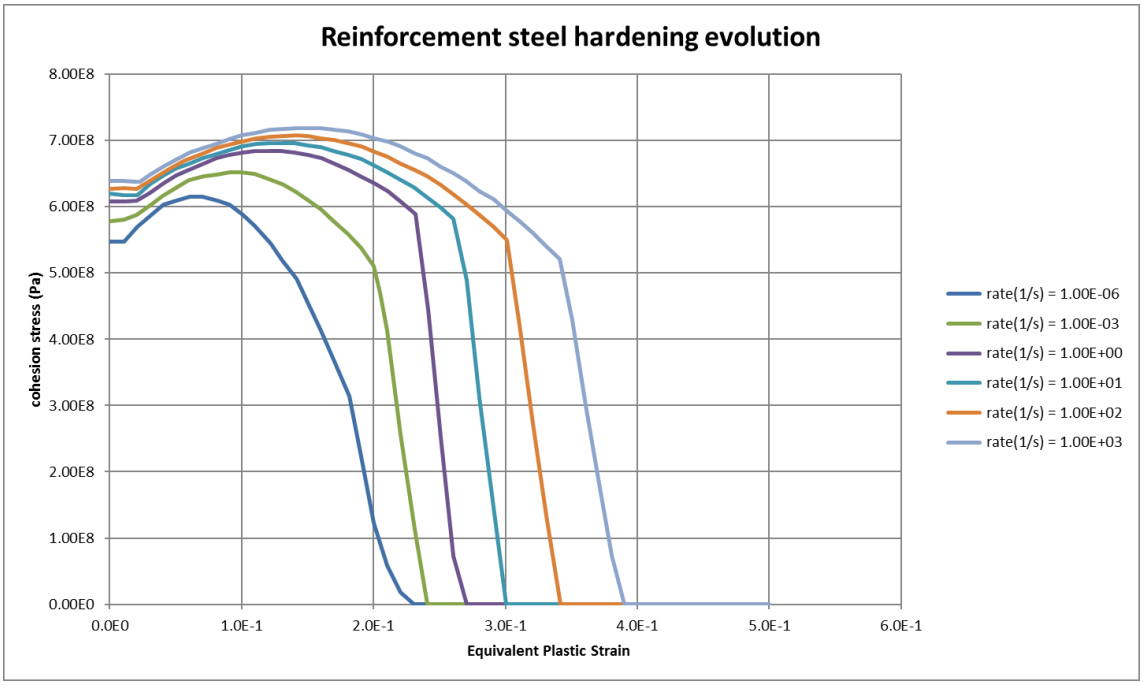

Figure 35 Reinforcement steel hardening/softening evolution for steel with 549 MPa yield stress and 618 MPa ultimate tensile strength at different rates.

5.4. Mesh Sensitivity Analysis

In order to realize an accurate size of mesh that yields mesh independent results, mesh sensitivity analysis is carried out. Experiment of the slab S3 is chosen for this analysis. In this experiment, the impactor did not perforate the slab, so it provides a chance to study the effect of mesh on the penetration depth of the impactor in addition to its velocity.

A mesh of 16 mm was chosen initially for the solid and beam elements, which was, then refined to finer meshes of 12 mm and 8 mm. The sizes mentioned are not exact but are used to refer to the three different meshes. The exact element size is adjusted a little automatically by Abaqus to fit the elements into the geometry while maintaining an aspect ratio close to 1. Table 7 includes the exact sizes and other details of these three meshes. The 16 mm mesh had five, 12 mm mesh had seven and 8 mm mesh had ten solid concrete elements across the thickness of the slab. The finest mesh (8 mm mesh) had 90250 solid elements for discretizing concrete and 1377 beam elements for discretizing the reinforcement whereas the coarse, 16 mm mesh, had

14553 solid elements for concrete and 792 beam elements in total. Figure 36 shows the 16 mm mesh and 8 mm mesh of solid elements for discretizing the concrete slab.

Table 7 Mesh Data for different meshes considered for mesh sensitivity Analysis

Slab S3	16 mm Mesh	12 mm Mesh	8 mm Mesh
Number of Nodes	14553	33677	102753
Solid Elements	11045	27783	90250
Beam Elements	792	972	1377
Solid Element Size	16.2 mm x 16.2 mm x 15.6 mm	12.06 x 12.06 x 11.14	8.0 mm x 8.0 mm x 7.8 mm

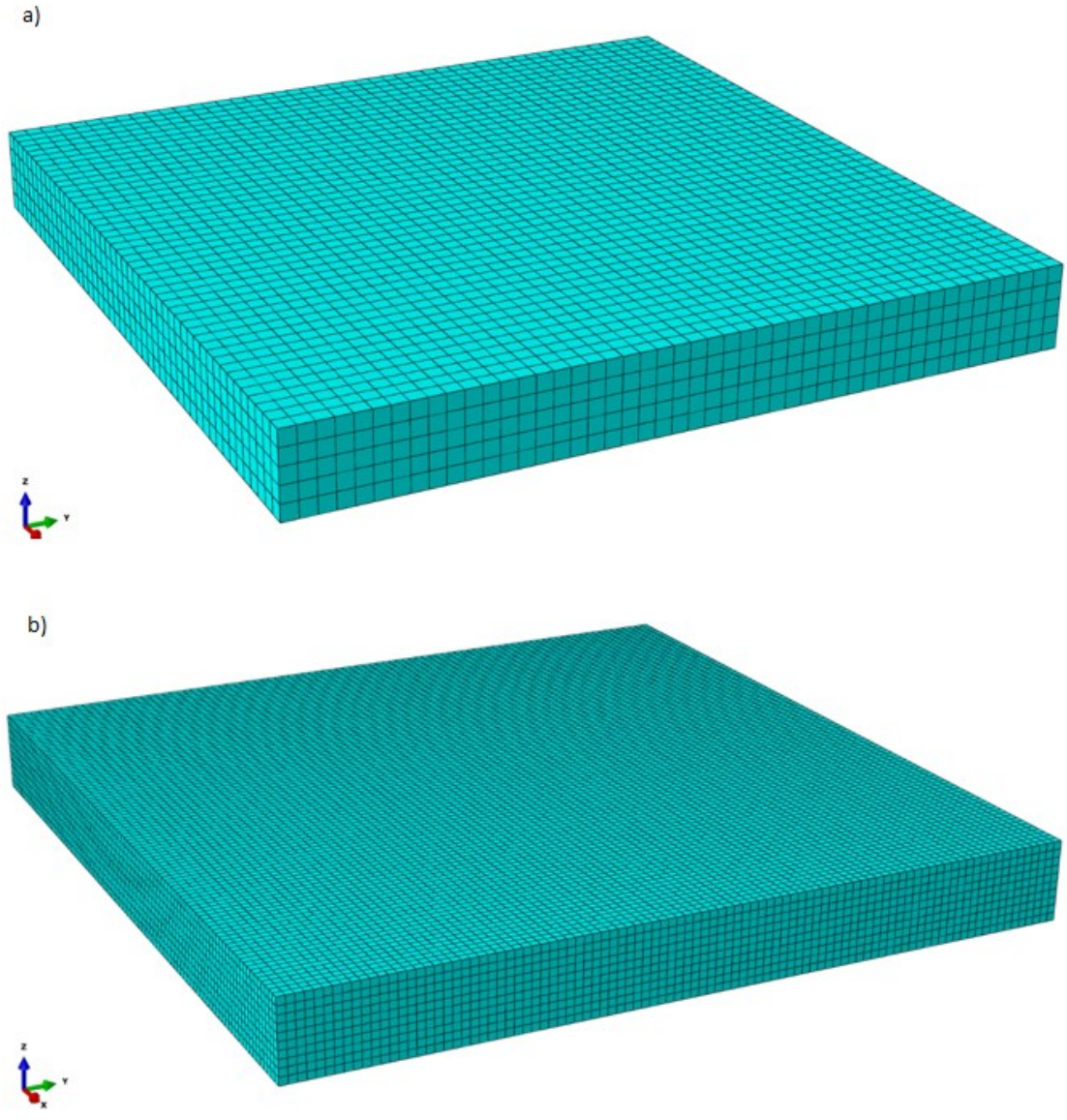

Figure 36 a) 16 mm Mesh b) 8 mm mesh

Figure 37 shows the transient velocity history of the impactor for experiment S3 from analysis using the chosen three different mesh sizes. The model seems to be moderately sensitive to the mesh size as can be seen from the difference in the profile of velocities. Overall velocity history seems to be converging as witnessed from less difference in velocity profile of impactor for 12 mm mesh and 8 mm mesh as compared to difference for 12 mm and 16 mm mesh. The impactor's velocity changes from a negative value to a small positive value for all the meshes

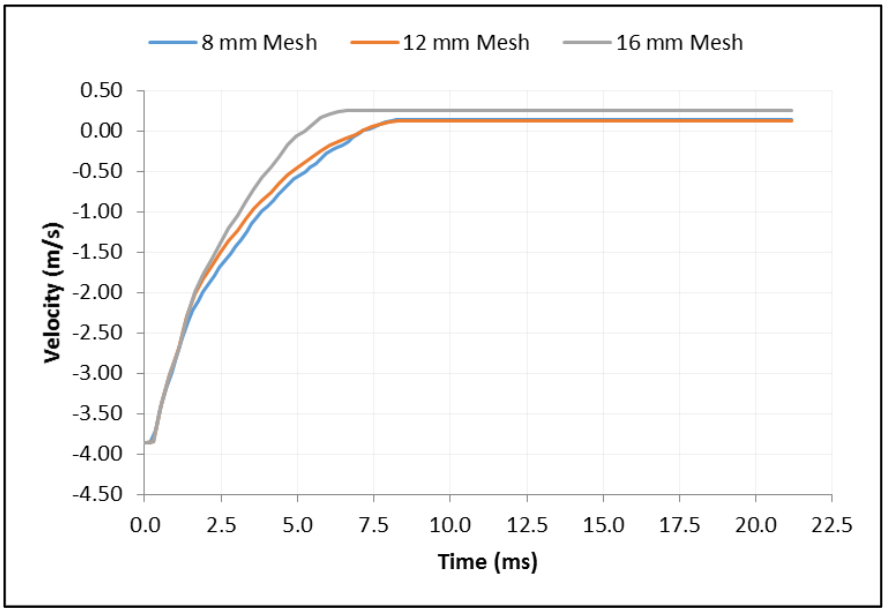

Figure 37 Influence of mesh size on the transient velocity history of the

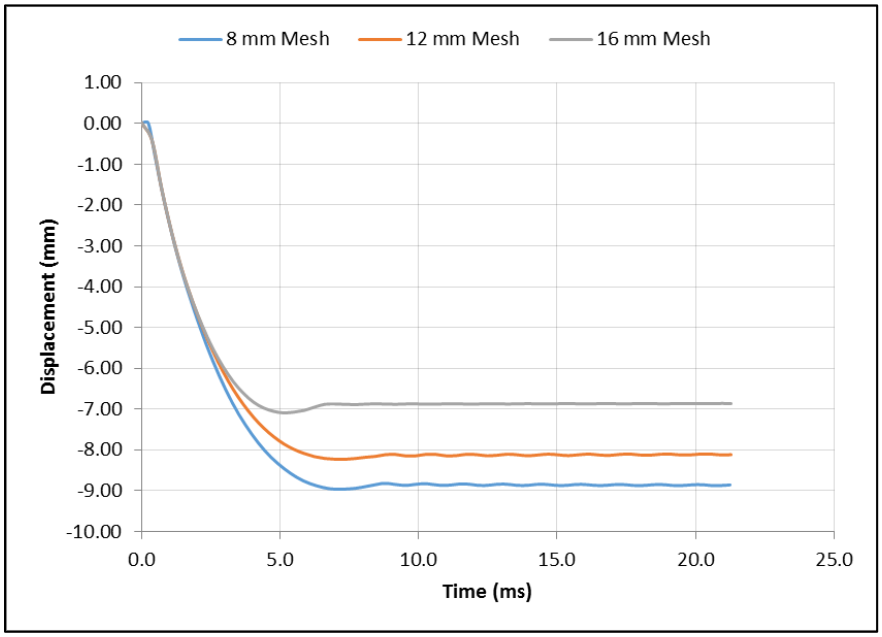

Figure 38 Influence of mesh size on the transient displacement of the mid-point on top surface of the slab

indicating a bouncing back of the impactor after which it has small constant velocity. For 16 mm mesh the impactor stops penetrating and bounces back at 5.2 ms whereas for the 12 mm mesh and 8 mm mesh this occurs near at the same time, i.e., 7.15 ms and 7.17 ms, respectively.

Another criterion to check the mesh sensitivity is the displacement of the mid-point on the top surface of the slab. It can be assumed as a measure of the penetration depth of the impactor. Figure 38 shows the transient displacement history of the mid-point on the top surface of slab for the three meshes. Analysis from 16 mm mesh shows maximum penetration of 7.1 mm at 5.13 ms whereas for 12 mm mesh and 8 mm mesh the maximum penetrations are 8.24 mm and 8.97 mm occurring at 7 ms and 7.33 ms. The difference in penetration for 16 mm mesh and 12 mm mesh is larger as compared to the difference for 12 mm mesh and 8 mm mesh. The overall shape of displacement history for 12mm mesh is also much closer to that for 8 mm mesh.

Based on the above observations, it could be concluded that the analysis from 8 mm mesh is relatively insensitive to the size of the mesh and hence this mesh size is used for the analysis of other tests as well. A more precise approach would be to perform sensitivity analysis for all the tests separately but owing to the less differences in the impact velocities, it can be assumed that the above mesh give accurate and mesh insensitive results for the other tests as well.

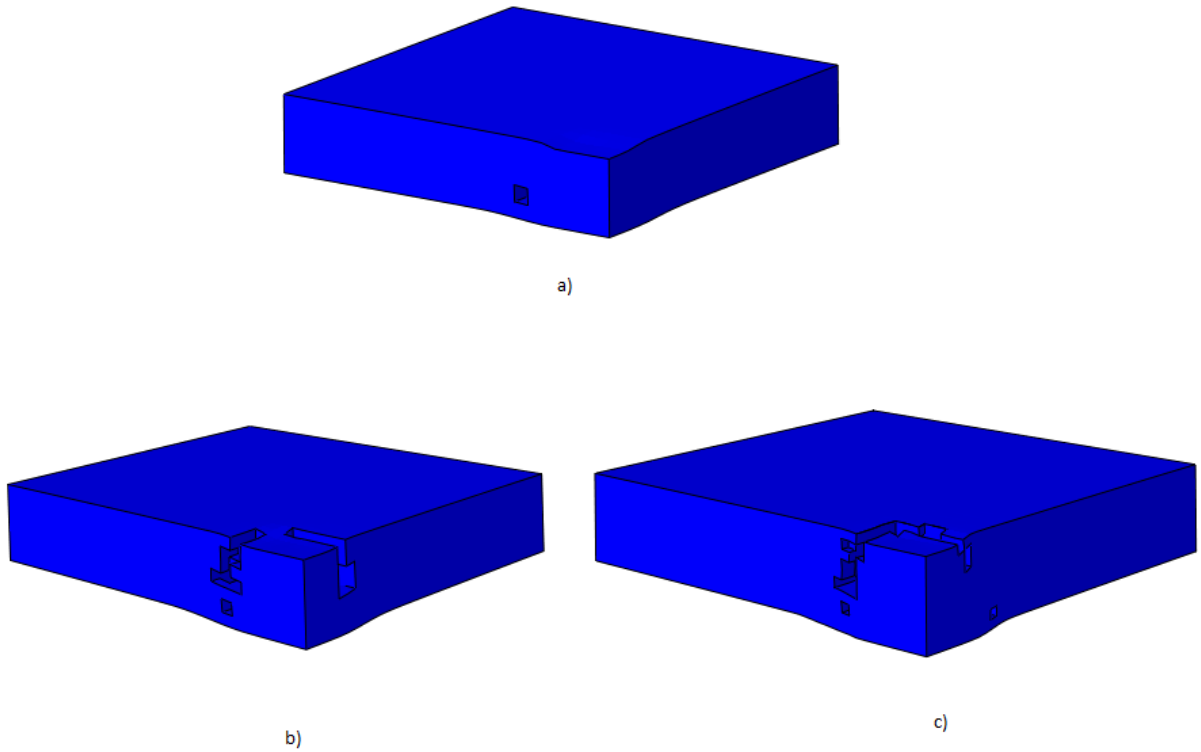

Figure 39 Qualitative convergence in terms of element deletion shown for a quarter of concrete slab a) 16 mm mesh, b) 12 mm mesh, c) 8 mm mesh.

Qualitative convergence in terms of elements deletion can also be verified for the chosen meshes from Figure 39. The figure shows a quarter section of the concrete slab without displaying the corresponding mesh to accurately compare the patterns left by the deleted elements. 16 mm mesh has little to no elements deleted, however the 12 mm and 8 mm meshes have quite similar volume of elements deleted indicating convergence.

5.5. Stability of the Solution

As discussed in Section 3.3, the Abaqus/Explicit solver uses an explicit time integration scheme. In such schemes the stability of the solution is warranted by keeping the time increment smaller than the time it takes for a dilatational wave to travel across the smallest element of the domain. Additional useful check on stability of an explicit solution is to check the energy balance of the system. For a stable solution, the conversation of energy should hold. The total energy of the system should be constant or close to constant over the time. A large change in the total energy can be a result of the time increment exceeding the stability limit and means an unstable solution. Another issue is to check the artificial strain energy of the system. Artificial strain energy of the system is the energy used to suppress the hourglass modes by the hourglass control formulations for the reduced integrated elements. This energy should be low as compared to the internal strain energy of the system.

Figure 40 shows various energy time histories for the analysis S3 slab. The total energy of the system is constant at 1.34 kJ indicating the energy conservation of the system. The artificial strain energy reaches its peak at 3 ms amounting to 10.7% of the internal energy after which it starts descending back to an average of about 8% of the internal energy. This ratio of artificial energy to the internal strain energy is considered well within the limits ensuring the stability of the solution.

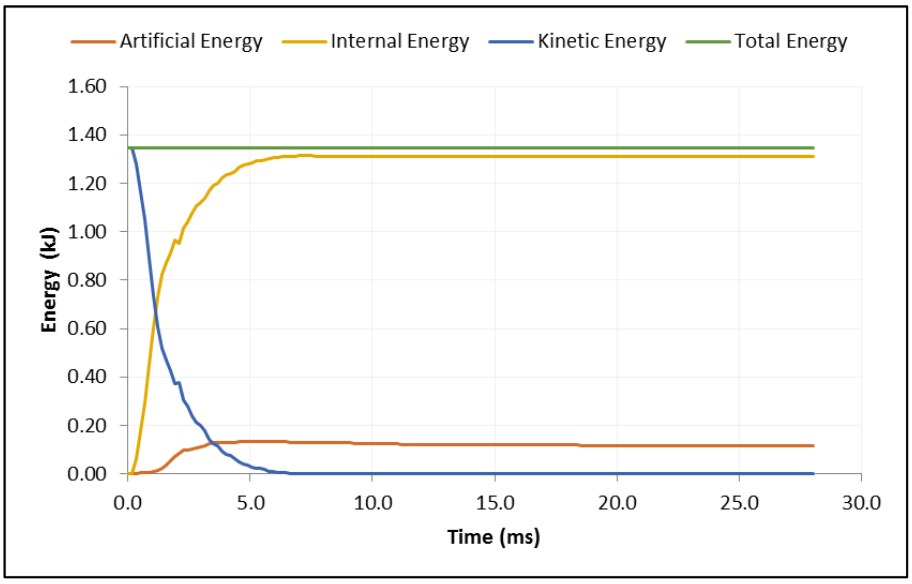

Figure 40 Energy Balance for the Slab S3 Impact Simulation

5.6. Comparison of the Experimental and Numerical Results

After the mesh sensitivity analysis, all the slabs were modelled with a mesh size of 8 mm. The impactor was given an initial impact velocity matching the experimental drop height. The total analysis time for the analysis was between 40 to 55 ms. A typical simulation run time was about one and half days for this mesh with relax stiffness hourglass control formulation. A lower run time was required when viscous hourglass control formulation was used since that introduces damping into the system and decreases the stability limit of the time increment. This section presents the comparison of results for the various impacts tests.

5.6.1. Slab S1

The impactor in the S1 slab experiment was dropped from 2.5 m. In the analysis, this drop height was converted into an initial velocity for the impactor, which equals 7 m/sec. The impactor perforated the concrete slab in the S1 slab experiment. The simulation results showed the similar response and perforation was occurred. Figure 41 shows the cut view of the slab in the middle at various time steps of the analysis. The impactor is shown perforating through the reinforced concrete of slab. The result contours on the slab shows the equivalent plastic strain in compression.

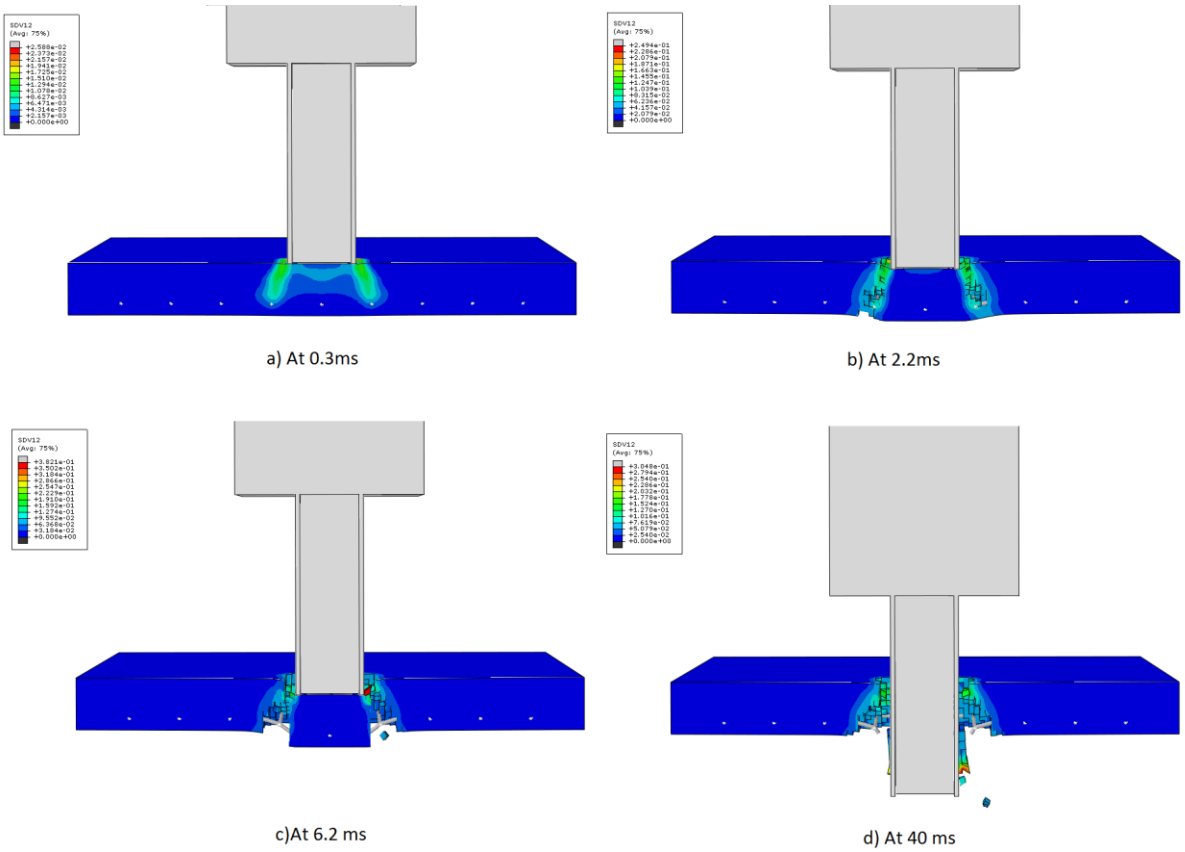

Figure 41 Model of S1 slab at different times of the analysis.

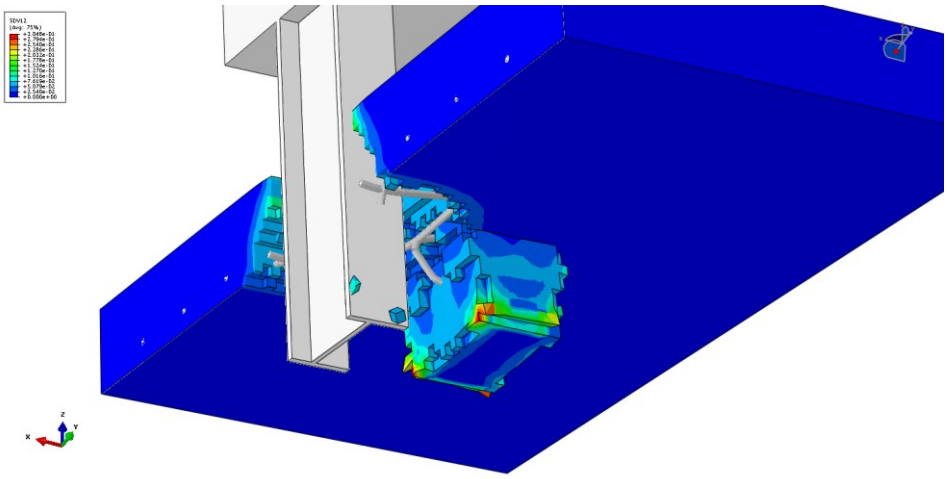

Figure 42 Isometric view of the S1 Slab model at 40 ms

The elements are deleted when the equivalent plastic strain has exceeded the element deletion criterion in compression. The figure shows that the impactor plugs out a concrete cone. The reinforcement is still embedded in the concrete. Upon further penetration, the reinforcement breaks near one boundary of the cone and hence the cone swings to the other side. Figure 41 with an isometric view shows the cone plug more clearly.

Figure 44 shows the comparison of the the velocity obtained from the analysis with the experimental velocity. The shape and slope of the velocity from the analysis matches very well with the experiment. In the analysis, the impactor perforates the slab at about 7.5 ms after which it continues to go through the slab unhindered at a constant velocity of 4.15 m/s. In the experiment, the perforation occured at almost the same time, however there is some hindrance to the impactor after the perforation, which can be seen in the form of decrease in velocity after the perforation. This hindrance perhaps is because of the scraping of the sides of the impactor with the adjacent concrete as it passes along or due to other losses in the impactor guides (Izatt *et al.*, 2009). The overall response however seems to have been well captured by the analysis. Figure 43 shows the qualitative comparison in the analysis and the experiment for the reinforcement. Since the velocity curves matches well, it could be argued that the element deletion criteria works well in the impact zone. However, the thin layer of scabbing farther from the impact zone cannot be captured by the model.

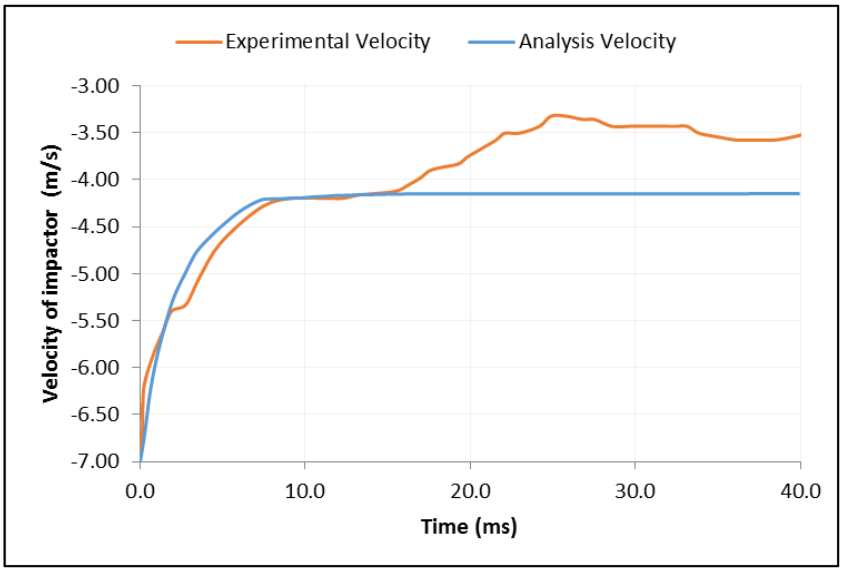

Figure 44 Comparison of the impactor velocity from the experiment and Analysis for Slab S1

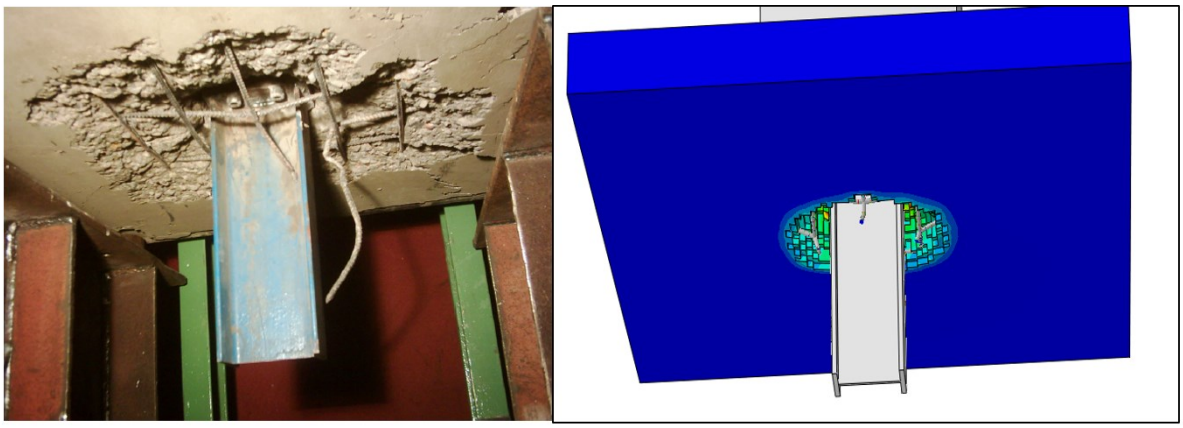

Figure 43 Perforation of I-section into the concrete slab from the experiment and the analysis.

5.6.2. Slab S2

In simulating the experiment of Slab S2, an initial velocity of 5.425 m/s was given to the impactor equivalent to the drop height of 1.5 m in the test. The analysis resulted in perforation of the impactor through the slab agreeing with the experiment. The impactor punched out a cone from the slab in the similar manner as in Slab S1. The model at different time steps of the analysis is shown in Figure 45.The velocity time history of the impactor is compared with the experimental velocity in Figure 46. The shapes of the curves have reasonable similarity. It can be seen that the impactor perforates the concrete slab at around the same time. The experimental velocity increases after perforation by a small amount, however, in the analysis, the impactor maintains a constant velocity and no such increase is evident.

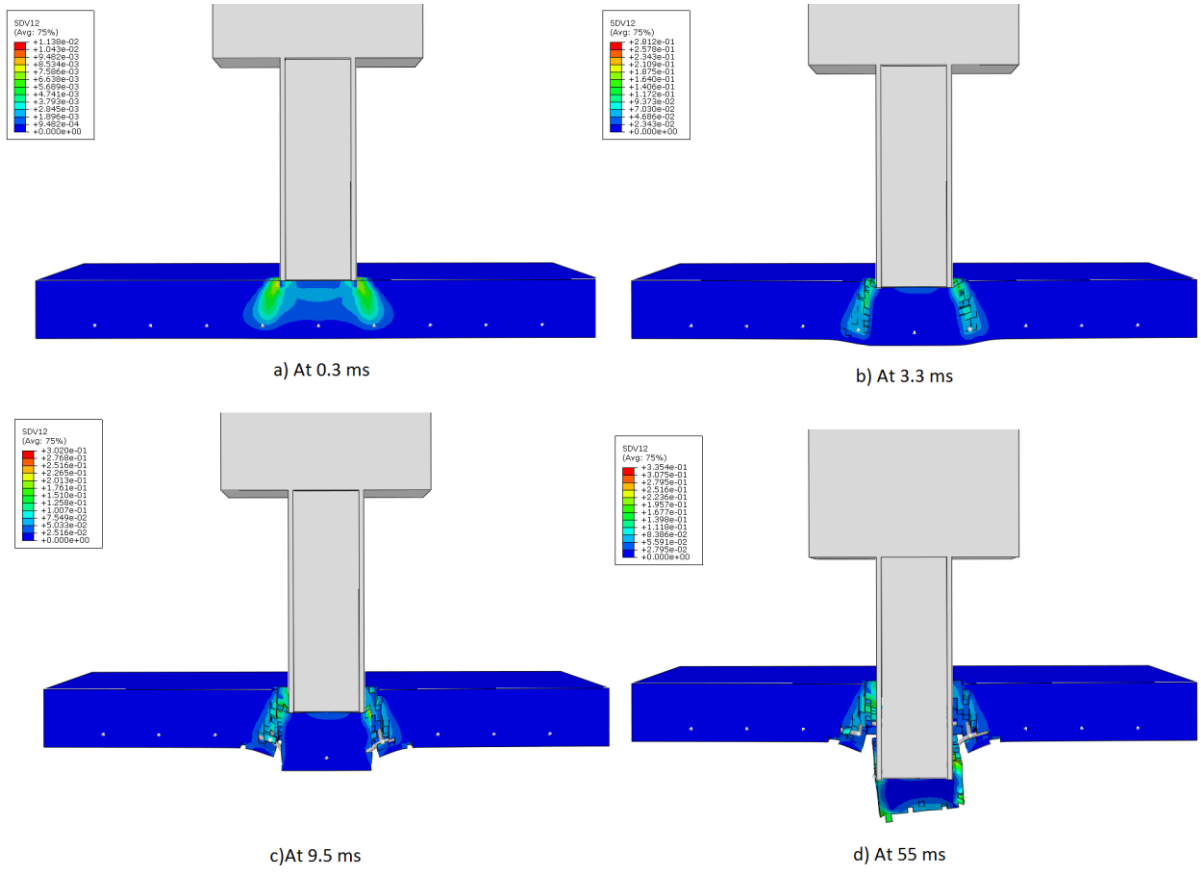

Figure 45 Model of S2 slab at different time steps.

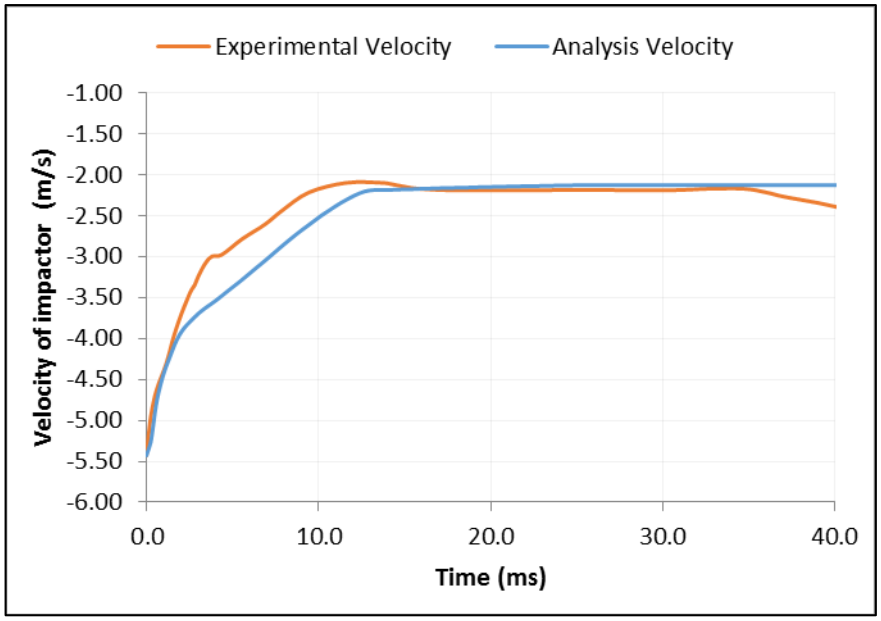

Figure 46 Comparison of the impactor velocity from the experiment and Analysis for Slab S2.

5.6.3. Slab S3

Analysis of Slab S3 also gave similar results in terms of perforation as from the experiment i.e., the impactor did not perforate the slab. The velocity time histories for the experiment and analysis are compared in Figure 48. A variation in the velocity histories, after the impactor stops penetrating, can be observed. In the experiment, the impactor rebounds around 10 ms and hence the greater velocity than zero as shown in the figure. However, in the analysis, the impactor rebounds by a very small amount and maintains a small constant velocity of 0.14 m/sec in the rebound direction. The reason perhaps for the lesser rebound in the analysis is that the impactor has been modelled as a rigid body. It should, however, be noticed that the velocity curves matches very well up to the point when the penetration stops and only deviates in predicting the rebound. This necessarily means that the material accurately predicts the penetration into

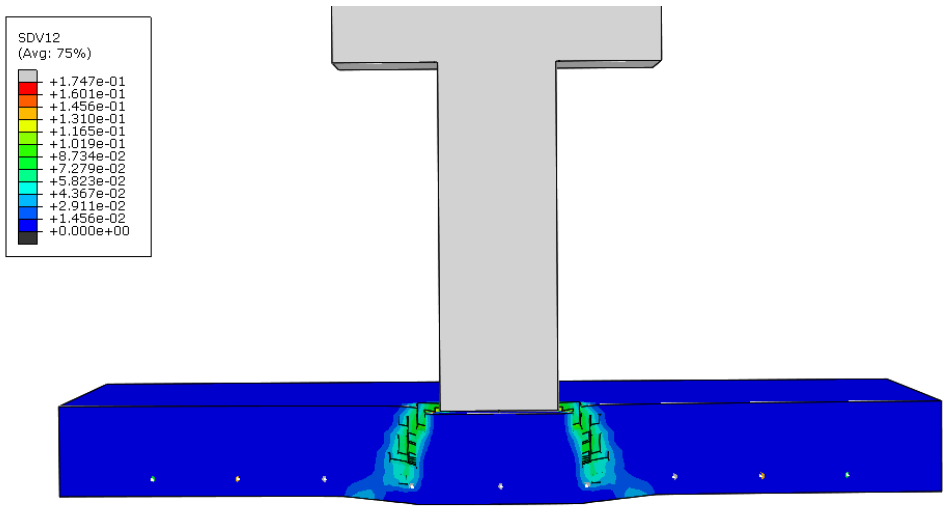

Figure 47 Slab S3 at the end of simulation showing no perforation.

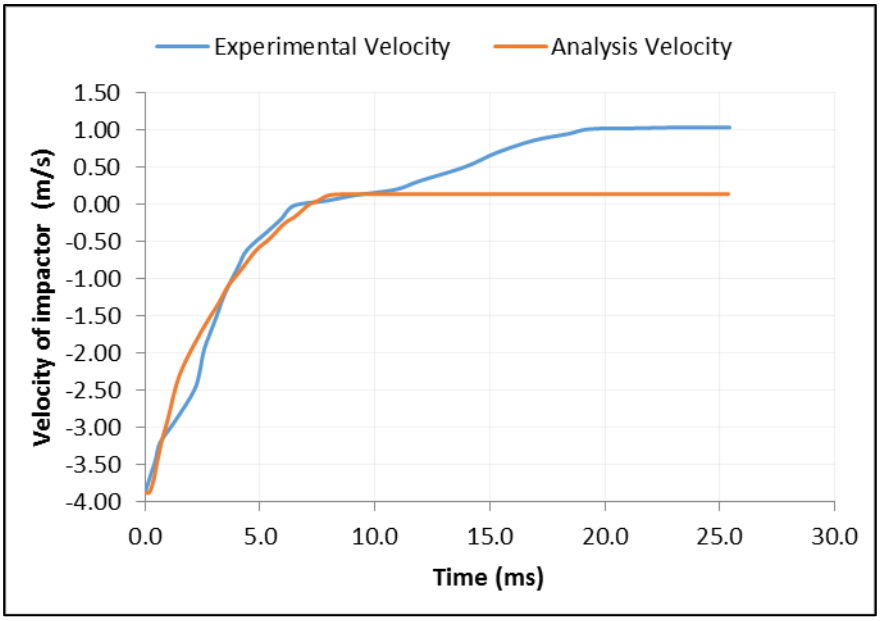

Figure 48 Comparison of the impactor velocity from the experiment and analysis for Slab S3.

the concrete slab. One limitation that was found is that no scabbing was observed in the distal face of the slab. Also it is worth mentioning that there is a different material deletion response when viscous hourglass formulation is used. For viscous hourglass formulation, a slight element deletion is observed at the distal face but that still is very local to the vicinity of the impact zone and the scabbing as observed in experiment, as shown in Figure 29, is not captured.

5.7. Conclusions

Based on the discussed results, it can be stated that the analysis gave results that matched significantly well with the experiment in terms of the impactor velocity. Some deviations were observed predominantly in terms of the residual and rebound velocity for slab S1 and S3 respectively. The probable reasons for such deviations have been stated and it can be argued that these does not affect the accuracy of the concrete material model. The dissipating velocity curve, before the deviations occur, matches the experimental curves very well.

The S2 slab and S3 slab have a very small difference of velocities in experiment. S2 slab was perforated and S3 slab was not. Since similar response was obtained as in the experiment from the analysis for these two slabs in terms of perforation, it can be argued that the model is very well capable of predicting the perforation of reinforced concrete slabs for low-velocity impacts.

One limitation that was observed is that the material model is not able to capture the scabbing at the distal face of the slab outside the vicinity of the impact zone for the S1 and S2 slabs. It also fails to capture the scabbing at the back face of the S3 slab in the impact zone. A slight scabbing at the back face of S3 slab was obtained when viscous hourglass controls were used but it was still not comparable with the experiment.

Since the reinforcement was present in the impact zone and the impactor did penetrate after the failure of reinforcement in that zone, the material model for reinforcement can also be said to have simulated identical response as in the experiment.

6. IMPACT ANALYSIS OF A TWO-LAYER SLAB

This chapter includes an impact analysis of a 150 mm thick two-layer reinforced concrete slab. This type of structure is more closely related to the construction industry context as the concrete slabs may typically have double layers of concrete rather than a single layer. The perforation limit, as a quantity, has been defined in the literature review earlier as the minimum thickness required for the target slab to prevent perforation. Another quantity that is related to the perforation is the ballistic limit and is defined as the minimum initial (impact) velocity required by the impactor to perforate through the target. This study investigates the ballistic limits for a 150 mm diameter cylindrical impactor with three different masses 250 kg, 500 kg and 1000 kg. A range of impact velocities needs to be considered for each mass to find out the minimum velocity that will perforate. The found ballistic limits are then compared with the empirical formulae to provide another layer of validation.

6.1. Specification of Two-layer Reinforced Concrete Slab

The slab size considered for this study is $3200\,mm \times 1600\,mm \times 150\,mm$. It consists of two layers of concrete; an upper 100 mm thick plain concrete layer and a lower 50 mm reinforced concrete layer. The upper layer has C35/45 strength class of concrete according to the Eurocode 2 and the lower layer has C40/50 strength class. The material properties for these strength classes of concrete are shown Table 8. The reinforcement is a 200 mm spaced mesh of 5 mm diameter reinforcement bars provided at the middle of the lower layer. The material properties of the reinforcement are same as in the validation study given in Table 5.

Table 8 Material properties for C35/45 and C40/50 strength classes of concrete.

Property	C35/45 concrete	C40/50 concrete
Density (kg/m^3)	2500	2500
Compressive strength (MPa)	43	48
Tensile Strength (MPa)	3.21	3.51
Poisson's ratio, ν	0.22	0.22
Elastic Modulus(GPa)	34.1	35.2

6.2. Numerical Modeling

Since the problem is symmetric about two horizontal axis, a quarter model of the problem was used in the numerical analysis. Langrangian formulation was used to model the three dimensional quarter of the slab with the size of $1600\,mm \times 800\,mm \times 150\,mm$. Two concrete layers were assigned to this single slab to represent the two concrete layers and assuming a perfect bond between the concrete layers. This assumption is based on the idea that the bond between the concrete layers would have little to no effect on the ballistic limit. Initially the slab was discretized uniformly with eight-noded hexahedron elements, C3D8R. But it was found out that the overall behavior of interest is quite local. So to increase the computational efficiency, a finer mesh is used near the impact zone and the farther region was discretized with courser C3D8R elements. The transition between the finer and courser elements was achieved by using reduced integrated 6-node linear triangular prism elements

C3D6R. The mesh size in the finer region is 12.5 mm in each direction. This gives 12 elements across the thickness which when compared to the mesh used in the validation study (10 elements across the thickness) is assumed to give relatively mesh insensitive results. The outer region mesh size was on average about 40 mm in the horizontal directions and 12.5 mm across the thickness. Figure 49 shows the mesh of the two-layered quarter slab model. The outer edge along the longer direction (along y-axis) of the quarter model was fully restrained whereas the shorter edge was free. It is worth mentioning that the boundary conditions on the shorter edge however would not have any significant effect on the perforation even if it's fully restrained because the response is quite local and that edge is far from that and so would have little effect on the results near the impact zone. The inner edges were assigned symmetry boundary conditions. The reinforcement is modelled using the discrete modelling approach this time and 2-noded beam elements are assigned to it.

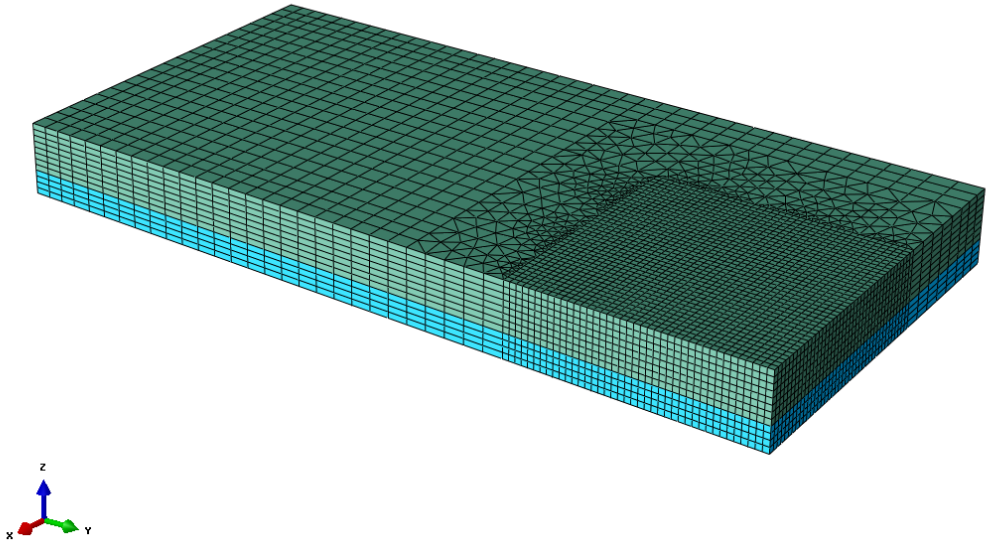

Figure 49 Mesh assigned to the quarter slab model.

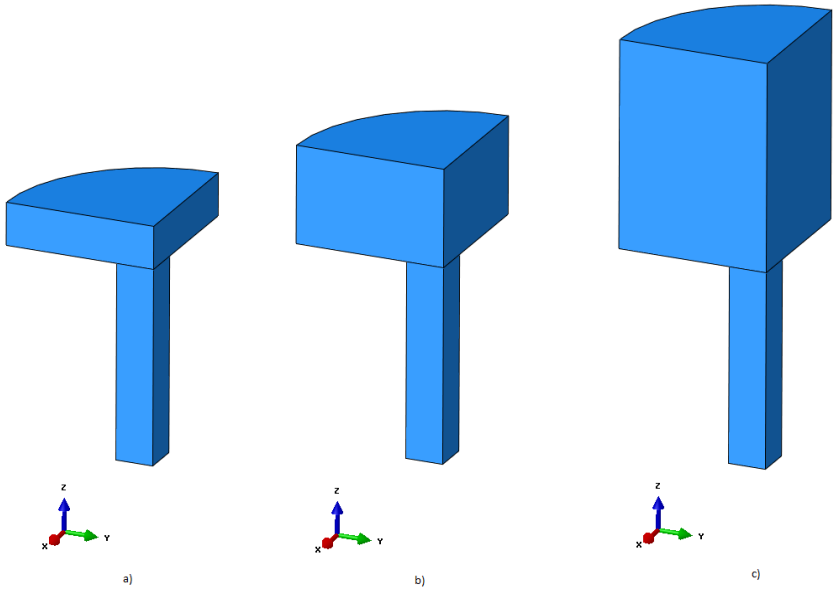

Figure 50 The quarter models of the impactors representing a) 250 kg, b) 500 kg and c) 1000 kg mass.

The quarter model of the impactor was modelled as a rigid body by assigning rigid body constraints. The mass of the impactor is calculated based on the assigned density which was 7850 kg/m^3 representing the steel. The impactor consisted of two quarter cylindrical parts. The lower part had a fixed size representing a quarter of 150 mm flat nosed cylindrical impactor. The upper part was dimensioned so as to equal the total mass of the impactor to the 62.5 kg, 125 kg or 500 kg which represents 250 kg, 500 kg and 1000 kg in the full model, respectively. Figure 50 shows the quarter models of these impactors.

6.3. Results

Explicit dynamics analysis is performed for various impact (initial) velocities to find the minimum velocity that will perforate through the two-layer slab for each slab. Since the analysis takes considerable time, the velocities were varied by minimum of 0.25 m/s. The ballistic limits for the different impactor that were found are given in Table 9. The curve fitted to these ballistic limits is shown in Figure 51.

Table 9 Ballistic Limits for various impactors

Impactor	Ballistic Limit (m/s)
250 kg Impactor	9
500 kg Impactor	6.5
1000 kg Impactor	4.75

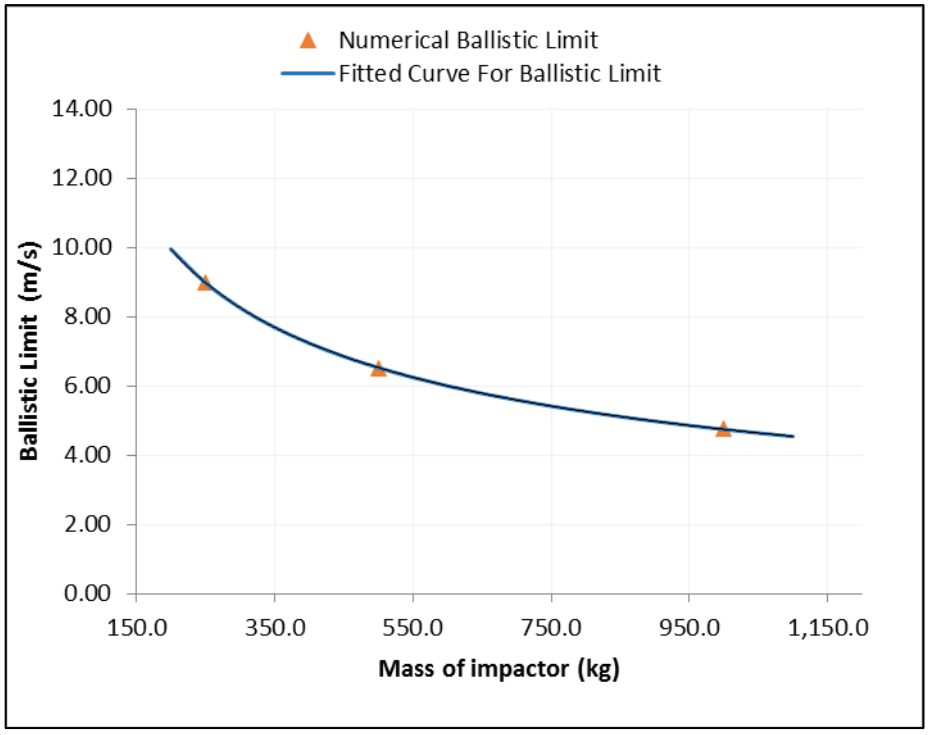

Figure 51 Numerical Ballisitic limit for three impactors and fitted curve.

Figure 52 shows the impactors perforating the two layered reinforced concrete slabs for the above ballistic limit velocities. The cone angle seems to be getting wider as the mass of the impactor increases. The difference is not that significant between the 250 kg and 500 kg but

for the 1000 kg impactor the cone angle is noticeable wider. The permanent deformations over the concrete top surface also increase for the increasing mass as shown in Figure 53. The maximum deformations observed are close to the impact region and roughly 2 mm, 3 mm and 5.5 mm for 250 kg, 500 kg and 1000 kg impactor respectively.

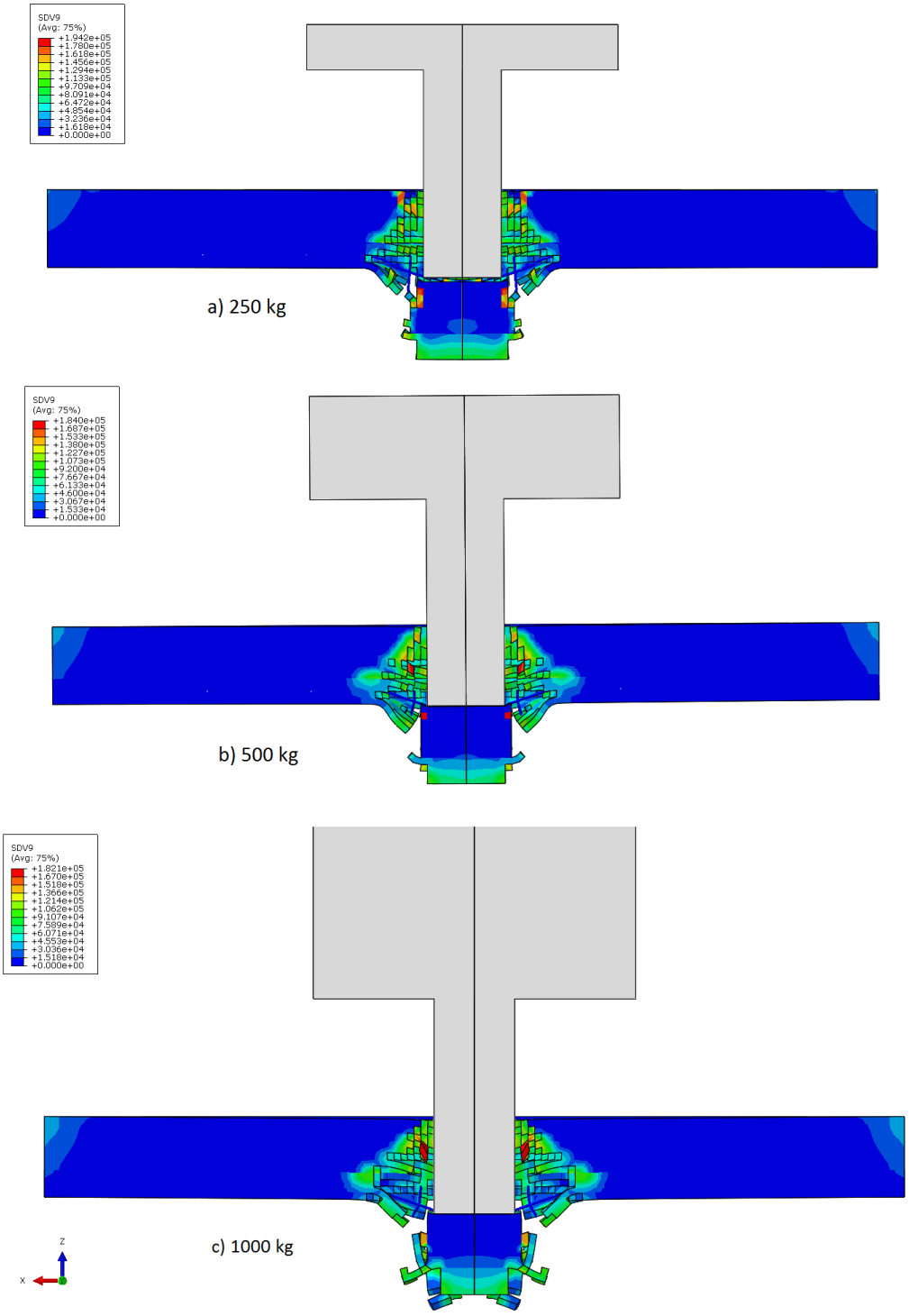

Figure 52 Perforation occurring in the concrete slabs impacted by a) 250 kg , b) 500kg , c) 1000 kg impactor

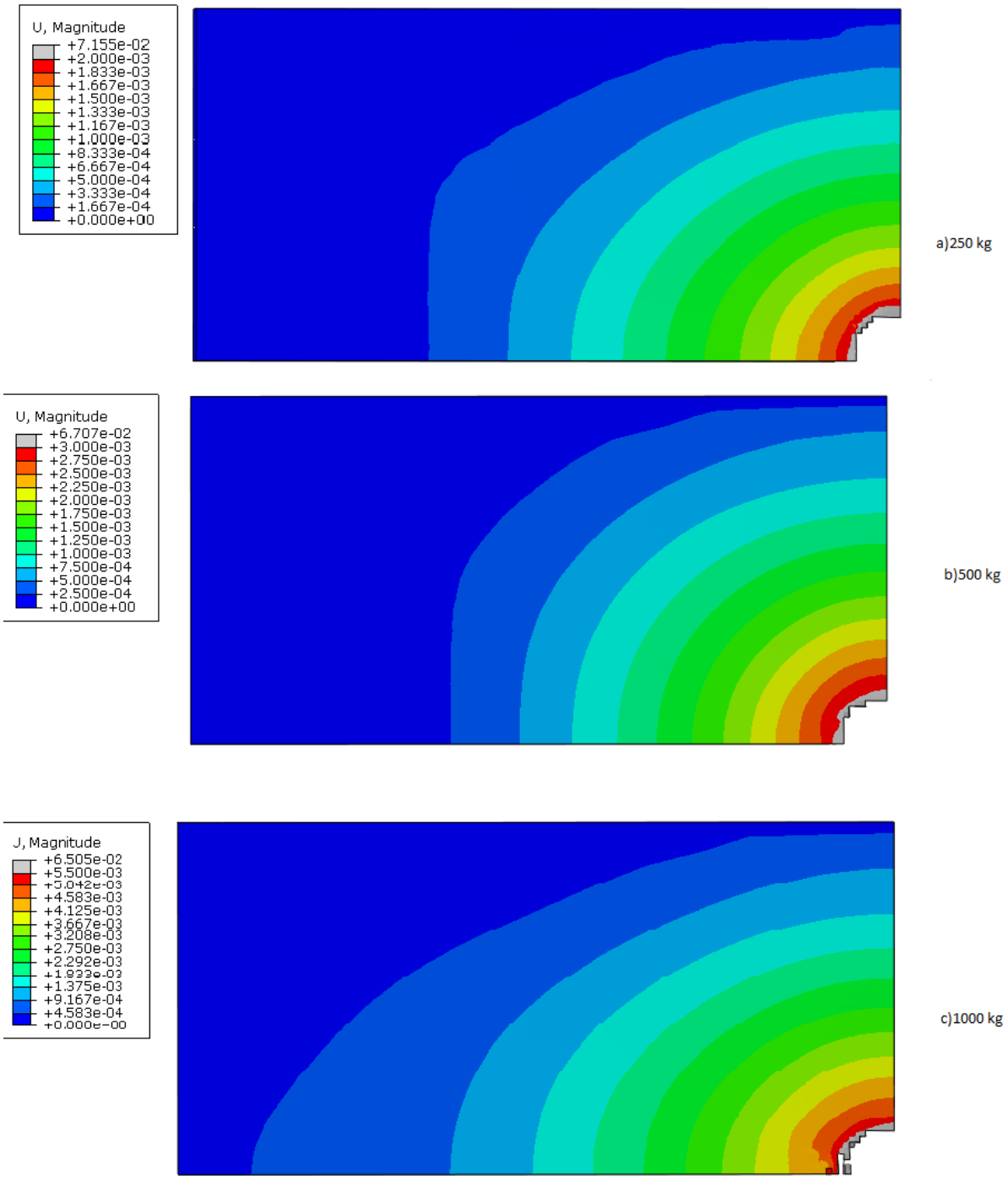

Figure 53 permanent deformation of the slabs top surface for different impactors.

6.4. Comparison with Empirical Formula

There are various formulae for predicting the penetration depth, perforation limit and ballistic limit developed over time based on the experimental and in some cases semi-analytical or analytical foundations. The modified NDRC (National Defense Research Committee) formula , developed in 1946, is one the most commonly used formula for the assessing the perforation limit of the reinforced concrete structures (NDRC, 1946). Originally, it was based on the experimental data of the smaller impactors with impact velocities greater than 150 m/s. (Barr, 1987) further developed this formula based on the extensive studies for the protection of the nuclear power plant structures to include the slow impact velocities as well and was called as UKAEA formula.

This section uses the ballistic limit suggested by the UK Atomic Energy Authority (UKAEA) empirical formula for comparison with the numerically obtained limits. The ballistic limit for the UKAEA formula was developed based on the CEA-EDF ballistic formula which has been found to provide better correlation with experimental tests for the slow velocity impacts (Sliter, 1980). (Algaard, Lyle and Izatt, 2005) have used this formula and was found to give better correlation with the experimental results. One another reason for the use of UKAEA ballistic limit formula is that it allows for the effect of reinforcement to be taken into the account as the reinforcement in our numerical model is about 0.065% which is very low as compared to the range for which the other empirical formulas are developed (0.3-1.6% each way). The formula is given as (Li *et al.*, 2005)

$$V = 1.3\,\rho_c^{\frac{1}{6}} f_c^{0.5} \left(\frac{p\,H_0^2}{\pi M}\right)(r+0.3)^{0.5} \tag{4.44}$$

where ρ_C is the density of concrete in kg/m^3.

f_c is the strength of concrete in Pa. It is taken as 37 MPa if f_c> 37 MPa

p is the perimeter of the projectile nose in meters.

H_0 is the thickness of the concrete target in meters.

M is the mass of the projectile in meters.

r is the percentage of reinforcement.

Figure 54 shows the comparison of the fitted curve for the ballistic limit based on the numerical results and the ballistic limit based on the empirical ballistic formula described above. The comparison shows quite good correlation between the empirical and the numerical curve, which further validates the finite element methodology.

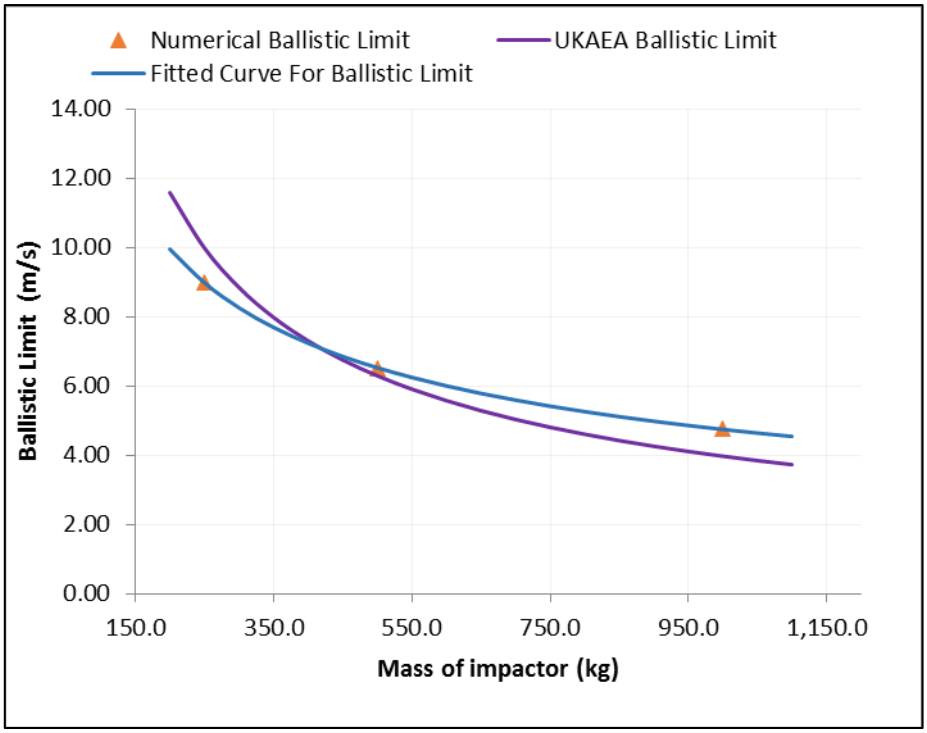

Figure 54 Comparison of the numerically obtained fitted curve for ballistic limit with the empirical ballistic limit curve.

7. CONCLUSIONS

This thesis presented a numerical procedure based on the finite element method to analyze the impact behavior of the reinforced concrete slabs. The study focused on the low-velocity and high-mass impacts. The main variable of interest was the perforation of the reinforced concrete slabs in regards to the safety in construction practices especially in construction of multi-storey buildings.

The numerical model used a modified concrete damage plasticity model for concrete and an elastoplastic damage model for the reinforcement. The procedure was validated by comparison with the experiments carried out at Heriot-Watt University. These experiments were more suited to the construction industry since they included low-velocity impacts. The experiments included three tests with a 198 kg steel I-section as impactor with impact velocities of 7.0 m/s, 5.4 m/s and 3.8 m/s. The model gives very accurate results in terms of perforation and velocity history of the impactor, validating the adopted procedure and material models. Slight deviations were observed in the residual and rebound velocity and the possible reasons for that are explained. Some limitations of the model in capturing the scabbing at the back face of the reinforced concrete slabs were observed and have already been discussed in section 5.7.

The validated numerical procedure is finally used for finding out the minimum velocity required by the impactor to perforate (ballistic limit) a 150 mm thick two-layer reinforced concrete slab. The two layers had different concrete strengths. Three impactors with weights 250 kg, 500 kg and 1000 kg with the same flat nose of 150 mm diameter were used. The found ballistic limits were then compared with ballistic limits based on the empirical formula suggested by UK Atomic Energy Authority (UKAEA). A very close correlation was found between the numerical and the empirical results, which further validates the numerical procedure adopted.

BIBLIOGRAPHY

ABAQUS. (2014). 'Version 6.14-1 Documentation', Providence, RI, USA: Dassault Systèmes Simulia Corp.

Algaard, W., Lyle, J. and Izatt, C. (2005) 'Perforation of Composite Floors', *5th European LS-DYNA User Conference*, (2), p. 3C–56.

Bamforth, P.,Chisholm, D.,Gibbs, J.,& Harrison, T. (2008) 'Properties of concrete for use in Eurocode 2',Surrey, UK: *Cement and Concrete Industry Publications.*

Barr, P. (1987) '*Guidelines for the design and assessment of concrete structures subjected to impact*', (SRD-R--439). United Kingdom

Belytschko , T., Liu, W.K. & Moran, B. (2000) '*Nonlinear Finite Elements for Continua and Structures*'. John Wiley & Sons Ltd., Baffins Lane. Chichester, West Sussex PO19 1UD, England.

Broadhouse, B.J. (1995) 'The winfrith concrete model in LS-DYNA3D' Tech. Rep. SPD/D(95)363, Structural Performance Department, AEA Technology, Winfrith Technology Centre.

Broadhouse, B.J. & Attwood. G.J. (1993) 'Finite element analysis of the impact response of reinforced concrete structures using DYNA3D', In K. Kussmaul, ed., *12th International Conference on Structural Mechanics in Reactor Technology*, Elsevier s Science Publishers B.V., University of Stuttgart, Germany.

Bischoff, P.;& Perry, S. (1991) 'Compressive behaviour of concrete under high strain rates', *Mater.Struct.*, 425-450.

Cadoni, E. and Forni, D. (2015) 'Strain rate effects on reinforcing steels in tension', *EPJ Web of Conferences*, 94, pp. 1–5. doi: 10.1051/epjconf/20159401004.

CEB (Comite Euro-International du Beton). (1990) 'CEB-FIP Model Code 90', Federation Internationale de la Precontrainte, Paris.

Chen, Y. and May, I. M. (2009) 'Reinforced concrete members under drop-weight impacts', *Proceedings of the Institution of Civil Engineers - Structures and Buildings*, 162(1), pp. 45–56. doi: 10.1680/stbu.2009.162.1.45.

Cook, R. D., Malkus, D. S. and Plesha, M. E. (1989) *Concepts and Applications of Finite Element Analysis*. 3rd ed. Jhon Wiley & sons, Inc., New York.

Eibl, J.;& Bachmann, H. (1993) 'Festigkeisverhalten von Beton unter dem Einfluenss der Dehngeschwindigkeit', *Massivbau Baustofftechnologie Karlsruhe, Universität Karlsruhe*.

Fedoroff, A., Kuutti, J. and Saarenheimo, A. (2017) 'A physically motivated element deletion criterion for the concrete damage plasticity model', in *Transactions, SMiRT-24 BEXCO Division III*. Busan, Korea.

Fedoroff, A. (2017) '*Continuum damage plasticity for concrete modelling*', VTT-R-00331-17.VTT

fib. (2010) 'fib Model Code 2010', Lausanne: International Federation for Structural Concrete.

Fullard, K. (1991) 'Interpretation of low velocity damage tests on concrete slabs', *Proceedings of the international conference on earthquake, blast and impact*, Manchester, UK,. p. 126–33.

Grote, D. L., Park, S. W. and Zhou, M. (2001) 'Dynamic behavior of concrete at high strain rates and pressures: I. experimental characterization', *International Journal of Impact Engineering*, 25(9), pp. 869–886. doi: 10.1016/S0734-743X(01)00020-3

Hillerborg, A., Modeer, M. and Pettersson, P. (1976) 'Analysis of crack formation and and crack growth in concrete by means of fracture mechanics and finite elements', *Cement Concrete Research*, (6), pp. 73–782.

Izatt, C. *et al.* (2009) 'Perforation owing to impacts on reinforced concrete slabs', *Proceedings of the ICE - Structures and Buildings*, 162(1), pp. 37–44. doi: 10.1680/stbu.2009.162.1.37.

Jabbar, A. *et al.* (2011) 'Reinforced Concrete Structures Under Impact Loads', (April).

Jankowiak, T. and Lodygowski, T. (2005) 'Identification of parameters of concrete damage plasticity constitutive model', *Foundations of civil and environmental ...*, (6), pp. 53–69. doi: 10.3390/app6090245.

Kennedy, R.P. (1976) 'A review of procedures for the analysis and design of concrete structures to resist missile impact effects', *Nuclear Engineering and Design*, 37, 183-203.

Klepaczko, J. R. and Brara, a. (2001) 'An experimental method for dynamic tensile testing of concrete by spalling', *International Journal of Impact Engineering*, 25(4), pp. 387–409. doi: 10.1016/S0734-743X(00)00050-6.

Kmiecik, P. and Kamiński, M. (2011) 'Modelling of reinforced concrete structures and composite structures with concrete strength degradation taken into consideration', *Archives of Civil and Mechanical Engineering*, 11(3), pp. 623–636. doi: 10.1016/S1644-9665(12)60105-8.

Kouhia, R. (2013), 'Betonin ajasta riippumattomat materiaalimallit', *Liikenneviraston tutkimuksia ja selvityksiä*.

Lee, J. H. and Fenves, G. L. (1998) 'Plastic-damage model for cyclic loading of concrete structures', *J. Eng. Mech. (ASCE)*, 124(8), pp. 892–900.

Li, Q. M. *et al.* (2005) 'Local impact effects of hard missiles on concrete targets', *International Journal of Impact Engineering*, 32(1–4), pp. 224–284. doi: 10.1016/j.ijimpeng.2005.04.005.

Li, Q. M. and Meng, H. (2003) 'About the dynamic strength enhancement of concrete-like materials in a split Hopkinson pressure bar test', *International Journal of Solids and Structures*, 40(2), pp. 343–360. doi: 10.1016/S0020-7683(02)00526-7.

Lubliner, J. *et al.* (1989) 'A plastic-damage model for concrete', *International Journal of Solids and Structures*, 25(3), pp. 299–326. doi: 10.1016/0020-7683(89)90050-4.

Malvar, L. J., and Crawford, J. E. (1998) 'Dynamic increase factors for concrete', Proc., 28th DDESB Seminar, DDESB, Alexandria, VA.

Malvar, L. J., and Ross, C. A. (1998) 'Review of strain rate effects for concrete in tension', ACI Mater. J., 95(6), 735–739.

Miyamoto, A., King, M.W., Fuji, M (1991). 'Nonlinear dynamic analysis of reinforced concrete slabs under impulsive load', ACI Structural journal 188(4): 411-419.

Mokhatar, S. N. and Abdullah, R. (2012) 'Computational Analysis of Reinforced Concrete Slabs Subjected to Impact Loads', *International Journal of Integrated Engineering*, 4(2), pp. 70–76.

NDRC (1946) *Effects of Impact and Explosion, Summary. National Defence Research Committee*. Washington, DC, Technical Report of Division 2, Vol. 1.

Nuclear Energy Agency Committee on the Safety of Nuclear Installations (NEA-OECD): 'Improving Robustness Assessment Methodologies for
Structures Impacted by Missiles (IRIS_2010)', *Final Report NEA/CSNI/R(2011)8, 2012*

Nuclear Energy Agency Committee on the Safety of Nuclear Installations (NEA-OECD): 'Improving Robustness Assessment Methodologies for
Structures Impacted by Missiles (IRIS_2012)', *Final Report NEA/CSNI/R(2014)5, 2014*

Ottosen, N.S. (1997) 'A failure criterion for concrete', *Journal of the Engineering Mechanics Deivision*, ASCE, 103, 527-535.

PAJĄK, M. (2011) 'The Influence of the Strain Rate on the Strength of concrete taking into account the experimental techniques', *Nanomechanics Science and Technology: An International Journal*, 2(3), pp. 231–253. doi: 10.1615/NanomechanicsSciTechnolIntJ.v2.i3.40.

Park, S. W., Xia, Q. and Zhou, M. (2001) 'Dynamic behavior of concrete at high strain rates and pressures: II. Numerical simulation', *International Journal of Impact Engineering*, 25(9), pp. 887–910. doi: 10.1016/S0734-743X(01)00021-5.

Rodríguez, J., Martínez, F. and Martí, J. (2013) 'Concrete Constitutive Model , Calibration and Applications', *2013 SIMULIA Community Conference*, pp. 1–15.

Ross, C.,Jerome, D.,Tedesco, J.,& Hughes, M. (1996) 'Moisture and strin rate effects on concrete strength', *ACI Mater. J.*, 293-300.

Schwer, L. (2010) 'An introduction to the Winfrith concrete model', *Schwer Engineering & Consulting Services*, (April), pp. 1–28.

Schwer, L. E. and Malvar, L. J. (2005) 'simplified cocrete modeling with *MAT_CONCRETE_DAMAGE_REL3', *Jri Ls-Dyna User Week*, pp. 1–14.

Scordelias, A. . and Ngo, D. (1967) 'Finite element analysis of reinfroced concrete beams', *ACI journal*, 64, pp. 152–163.

Shirai,T.,Kambayashi,A.,Ohno,T.,Taniguchi,H.,Ueda,M.,Ishikawa,N. (1997) 'Experimental and Numerical Simulation of Double-Layered RC Plates Under Impact Loading' *Nuclear Engineering and Design* 176: 195-205.

Shiu, W., Donze, F. V. and Daudeville, L. (2009) 'Discrete element modelling of missile impacts on a reinforced concrete target', *International Journal of Computer Applications in Technology*, 34(1), p. 33. doi: 10.1504/IJCAT.2009.022700.

Sliter, G. E. (1980) 'Assessment of empirical concrete impact formulas', *Journal of the Structural Division, ASCE*, 106,(No. ST5), pp. 1023–1045

Tavarez, F.A., (2001), 'Simulation of Behavior of Composite Grid Reinforced Concrete Beams Using Explicit Finite Element Methods', *Master's Thesis*, University of Wisconsin-Madison, Madison, Wisconsin

Terranova, B., Schwer, L. and Whittaker, A. (2017) 'wind-borne missile impact on reinforced concrete nuclear structures : a parametric study', (2015).

Vepsä, A. *et al.* (2012) 'Impact tests for IRIS 2010 benchmark exercise', *Journal of Disaster Research*, Vol.7(No.5.).

Weerheijm, J. and Vegt, I. (2010) 'The dynamic fracture energy of concrete. Review of test

methods and data comparison.', *7th International Conference on Fracture Mechanics of Concrete and Concrete Structures (FraMCos-7)*.

Wu, Y. *et al.* (2015) 'Numerical Modeling of Concrete Using a Partially Associative Plasticity Model', 141(2002), pp. 1–24. doi: 10.1061/(ASCE)EM.1943-7889.0000952.

Wu, Y., Crawford, J. E. and Magallanes, J. M. (2012) 'Concrete Constitutive Models', *12th International LS-DYNA Users conference*, (1), pp. 1–14.